OPTIMAL FLOATING PLATFORM DESIGN FOR OFFSHORE ENERGY SYSTEMS

by

Chandler Shaw Cain

A Thesis

Submitted in Partial Fulfillment of the

Requirements for the Degree of

Master of Science

Major: Mechanical Engineering

The University of Memphis

May 2024

Abstract

A comprehensive study was performed on the hydro-structural design exploration of floating platforms for offshore energy systems using shape parameterization and dynamic system design optimization techniques. The study aims to develop a novel design framework that optimizes the structure of the platform for stable dynamic responses to ocean waves, ensuring that the motion of the platform as well as its acceleration are reduced when compared to the simple designs currently employed, while ensuring satisfactory geometrical constraints. The study delves into the free-form design of the outer columns of the floating platform beyond conventional predefined shapes to enhance the overall performance of the system. The design utilizes a parameterization based on free-form spline interpolation for the outer shape of the hull and fixed-shaped pontoons to connect to the central structure where the energy-generating device (e.g. wind turbine) is installed. The study employs hydrostatic, hydrodynamic, and time-domain structural dynamic simulations within a monolithic multidisciplinary design optimization formulation to evaluate the overall dynamic responses of floating platforms. Overall, this study provides valuable insights into the hydro-structural design of the floating platforms for offshore energy systems. The optimal shape of the outer column suggests that the concave design enhances dynamic performance by effectively reducing the span-wise footprint of the platform. The results offer design considerations for floating platform hull developers to create robust designs that can withstand harsh metocean conditions while also providing more incentive for increased deployment of offshore energy production utilizing these platforms. Floating platforms are the most expensive method for providing a platform for offshore energy production, but the optimization of the shape shows increased stability and a further incentive to deploy this type of platform. The findings obtained from the optimization solutions suggest the need for advanced design exploration and shape optimization of the floating platform hull, including the pontoons and the central structure for optimal performance. The study also suggests employing manufacturability constraints and wave loadings in all possible directions to reflect real-world operating conditions of floating platforms.

Table of Contents

List of Tables

List of Figures

Abbreviations

BEM   boundary element method
DOF   degree-of-freedom
TLP   tension-leg platform

Chapter 1

Introduction

As energy demand has increased drastically over the last few decades, the critical significance of large-scale energy production has become increasingly evident. However, this growing demand has led to heavier reliance on fossil fuels, exacerbating pollution and waste problems [1]. While fossil fuel-based energy productions continue to to further debilitate our planet, they still remain more economical than environmentally friendly alternatives. Consequently, substantial efforts have been dedicated to lower the cost of renewable and envirnomentally friendly energy options in order to mitigate the environmental impact [2–4]. These efforts have sparked increased focus on various forms of new renewable energy sources, and one field among these efforts is offshore energy production [5]. Offshore energy production capitalizes on the expansive open ocean space to harness Earth's natural energies, including wind, wave, tidal, and thermal sources. A key challege shared by across these types of energy sources is how to deploy them in the ocean. This study aims to cost-effectively deploy these systems, particularly offshore wind energy systems, which is among the most studied recently [6, 7], on the ocean by emphasizing the development of optimal floating platforms. However, the findings of this research can be applicable to other ocean surface-based energy production methods.

Wind energy stands as a significant renewable energy sources, second to photovoltaic systems [8]. While some other offshore energy systems, such as thermal or ocean current energy systems, can be directly installed on the sea bed, the primary method for deploying offshore wind energy is on platforms [9]. These platforms may have various forms, but can broadly categorized into two types: either fixed platforms attached to the bottom of the sea bed or floating platforms. Each type has distinct advantages and disadvantages [10, 11]. Fixed platforms, requiring extensive underwater drilling and construction efforts for each installation, are suitable for areas with shallow water, typically closer to shorelines. In contrast, floating platforms, requiring significantly higher level of engineering, offer more flexibility as they are not constrained by the

depth of water.

Floating platforms must be secured within designated locations, and this is typically accomplished through the use of mooring lines anchored to the sea bed. The specific mooring method varies depending on the type of floating platform used [12]. The variety of floating platform options encompasses barge, semi-submersible, spar-buoy, tension-leg platforms (TLPs), among others. Each platform type offers distinct benefits and drawbacks, and comparison among these options is out of scope, as this research specifically concentrate on the design of TLPs. Although floating platforms provide much easier deployment, it is by far the most expensive method for deploying offshore energy systems, due to various technical challenges higher associated cost factors [13]. One constraint comes in the form of production. These floating platforms vary in length, spanning from 50 to over 100 meters and weighing approximately 1,000 tonnes or more, necessitating a large-scale production facility (such as a large working deck) at port locations, significantly limiting the choice of production facilities [14]. The inability to transport these large-scale structures, along with the limited availability of production plant, sharply contrasts with the more widespread production for land-based wind turbines in terms of both cost and availability. Towing platforms to their installation sites demands specialized vessels for transportation and offshore assembly connecting them to the mooring lines attached to the anchoring points on the sea bed [15]. The cumulative effect of these factors leads floating offshore wind energy expensive.

TLPs are often overlooked as potential floating platform options for the offshore energy systems due to various constraints, which results in a preference for spar-buoy or semi-submersible counterparts. The primary drawbacks of TLPs stem from their high cost in the mooring systems compared to other floating platforms. This is attributed to the relatively high tension force applied to the mooring lines, necessitating larger anchoring mass and a sturdier fairlead structure [16]. However, TLPs provide key benefits that should not be overlooked when compared to their counterparts. TLPs offer significantly enhanced stability due to their constrained pitching and rolling degrees-of-freedom (DOFs), resulting in reduced movement in

unfavorable directions when subject to wind and wave loadings on the floating platform [17].

However, this enhanced stability comes with the caveat of being the most expensive floating

platform design presently in use.

Not only do the floating platforms require towing out to the deployment site, but it also

requires the addition of floating platforms attached to the platform during deployment [18].

Doing this alleviates any loading placed on the floating platform while the mooring lines and

wind tower are being attached. Although they are more expensive, TLPs have even more benefits

[19]. Most floating platforms move around during loading, but TLPs have the benefit of resisting

heave motion far more than their floating platform counterparts [20]. This helps the wind turbine

to harness more of the energy being produced by the wind instead of being pushed around and

converting that energy into motion. They also cut down on a lot of material, being the most

resource efficient floating platform currently used in operation. A few more unmentioned benefits

make TLPs very desirable for this study and will be the focus of our research moving forward

[21].

The purpose for this study is to determine whether or not there is an even more efficient

form of the TLP than those that are currently deployed. TLPs provide so many benefits that

could be further enhanced through a design optimization study to attempt to optimize the outer

shape of the floating platform. In many engineering design problems where simple traditional

shapes are commonly used, creative parameterization to create non-conventional designs without

human-imposed assumptions may enhance system performance by orders of magnitude beyond

what was generally available with traditional forms [22, 23]. This study employs the use of a

design optimization algorithm to model the outer hull of a TLP previously developed by prior

research and attempt to modify the geometry of the outermost points along the frame to minimize

vertical movement of the floating platform during stochastic loading. Load analysis is performed

every time step in a given time frame and analyzed to facilitate the performance of the shape of

the outer face on each of the columns for the floating platform. The design was then modified

and subjected to repeat analysis until a convergent design was reached that exhibited the desired

improvements.

The main body of this thesis is divided into 4 chapters. Chapter 2 covers the literature reviewed for filling out the design space as well as gaining a good understanding of what has been developed before. Chapter 3 describes the methodology used in order to perform the research and analyze the TLP in question. The results and discussion have been relegated to Chapter 4 with Chapter 5 being the final conclusion of the work as well as a look towards possible future contributions. Some of the methodologies, results, and findings described in this thesis were presented at the ASME 2023 International Mechanical Engineering Congress and Exposition [24].

Chapter 2

Background and Literature Review

Wind turbines are one of the most accepted forms of renewable energy, second to photovoltaic, used in the United States [25]. This means that the widespread adoption of these systems has led to various in-depth research particularly on interactions between the rotor blades, nacelle, and tower and the wind loading experienced during operation [26–28]. Designing efficient rotor blade design alone requires significant efforts in theoretical, computational, and experimental research on atmospheric turbulence, aeroelasticity, structural dynamics, materials, among many others, and considerable advancements have been made through these research efforts [29, 30]. A large majority of the energy calculations behind wind turbine effectiveness are directly derivative of the size of the blades [31]. Due to the shear effect of wind flow against the surface (ground or water), larger wind turbines provide enhanced energy generation efficiency [32]. Figure 1 shows the relationship and the increase in size possible with off-shore wind turbines. However, with land based turbines are limited in their size, capped at the maximum of 100 m in blade length with the most recent technical advancements. Due to this limitation, numerous engineers and researchers sought locations that would not restrict the size of the wind turbine, such as the Great Lakes and open ocean spaces [33].

Due to the substantial available spatial resources with fewer constraints, designers have significantly greater freedom in design exploration of new and emerging renewable energy technologies out on the ocean [34]. This upscaling trend is especially apparent for wind energy, which has a rotor diameter over 240 m with recently developed turbines with 15 MW scale and beyond [35]. Deployment of these towers can be done in a variety of ways, although the main difficulty shared across all deployment methods is construction out on the ocean [36]. Fixed foundations, such as monopile or truss, can also be considered [37]. These towers provide a rigid solution to placing wind turbines but only feasible for certain conditions. These foundations are exclusively designed for use with wind turbines and are confined to shallow water depths,
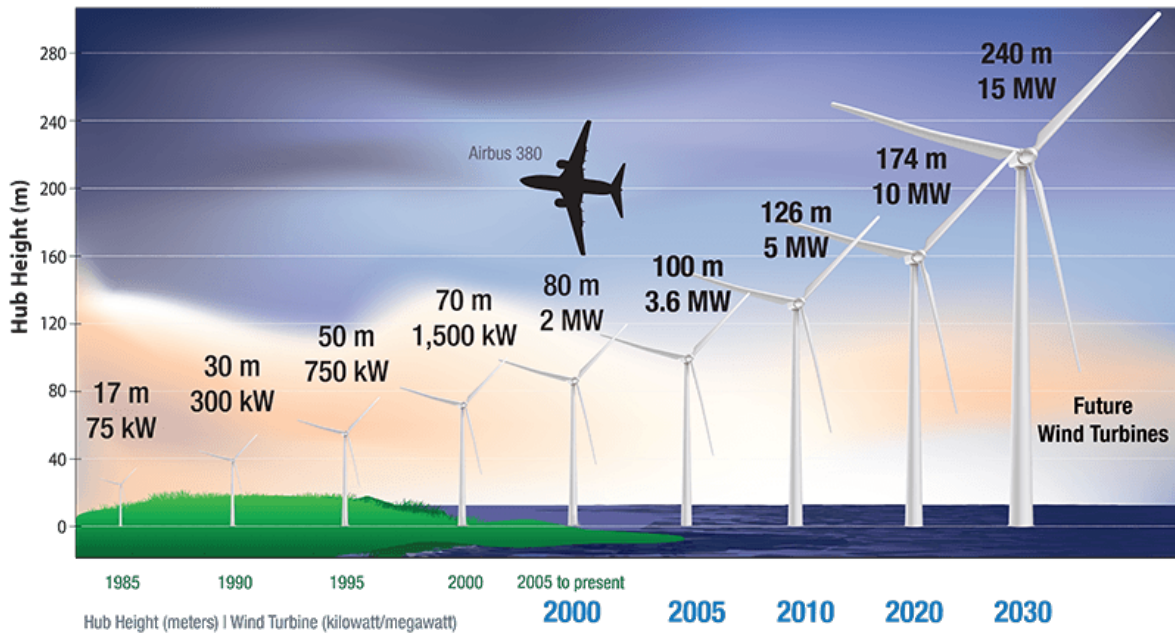
Figure 1: Turbine Height Variation [42]

typically below 30 meters. However, numerous desired locations have water depths that surpass this limit, which eventually requires introduction of offshore floating platforms [38, 39]. Floating platforms avoid these limitations and allow much greater flexibility when it comes to deployment of experimental technologies [40]. Deployment depths for these floating platforms is also significantly increased compared to their fixed tower counterparts [41].

There are a large variety of offshore floating platform options available [43]. Barges are ship-like structures that tow out equipment to the desired location [44]. They move with the waves to avoid over stressing the structure but are typically fitted with heave plates to minimize the bulk of motion. Spar-buoy platforms have a lengthy cylindrical body submerged in the water with a ballast mass at the bottom of the platform. The platform is moored with slack or semi-taut lines connected to the anchoring point of the sea bed [45]. Semi-submersible platforms are the most commonly deployed design implementing a tactic of minimizing surface area contact with the water but maximizing the volume [46]. The last type of floating platform is the TLP, which is

6

the focus of this research study [47, 48]. TLPs are platforms constructed using the least material and volume possible to provide the most stable platform possible. Unlike the other types of platforms, once the turbine is installed, the center of gravity rises and this operates in tandem with the buoyancy center and allows the platform to remain stable. The platform is then firmly secured to the ocean floor with tight mooring lines [49]. These mooring lines are tensioned cables that keep the platform mounted in place with a little room for motion as the tension increases on one leg and decreases on another until a tensile limit is reached and the floating platform is constrained.

TLPs have had a relatively short history of study compared to the other floating platform counterparts. However, numerous studies have been conducted to improve their design [50]. Early investigations primarily focused on design development [51]. Some novel design concepts were initially explored to clearly understand underlying mechanics of TLPs [51–53]. Most designs developed over time consistently converged to multi-column designs, and among them, three outer-column TLPs with a central column for payload attachment became the most popular options for offshore renewable energy applications. This particular configuration provides outstanding stability and easy mooring line attachment capability within a small footprint [54].

There are multiple types of designs when it comes to these wind turbines, such as horizontal wind turbines or vertical wind turbines [55]. The differences between these two are given in Fig. 2. For the purpose of this study, horizontal wind turbines will be the largest focus. The amount of energy produced by these offshore turbines is highly dependent on the size of the blades, as mentioned earlier [32]. This means that as the turbines become larger and larger, the floating platforms being deployed are required to become larger and larger to accommodate them. The size of the platforms ranges greatly depending on the size of the blades for the turbine which means that every square inch of the platform needs to be as optimal as possible to further increase the feasibility of their inclusion in the offshore market [56].
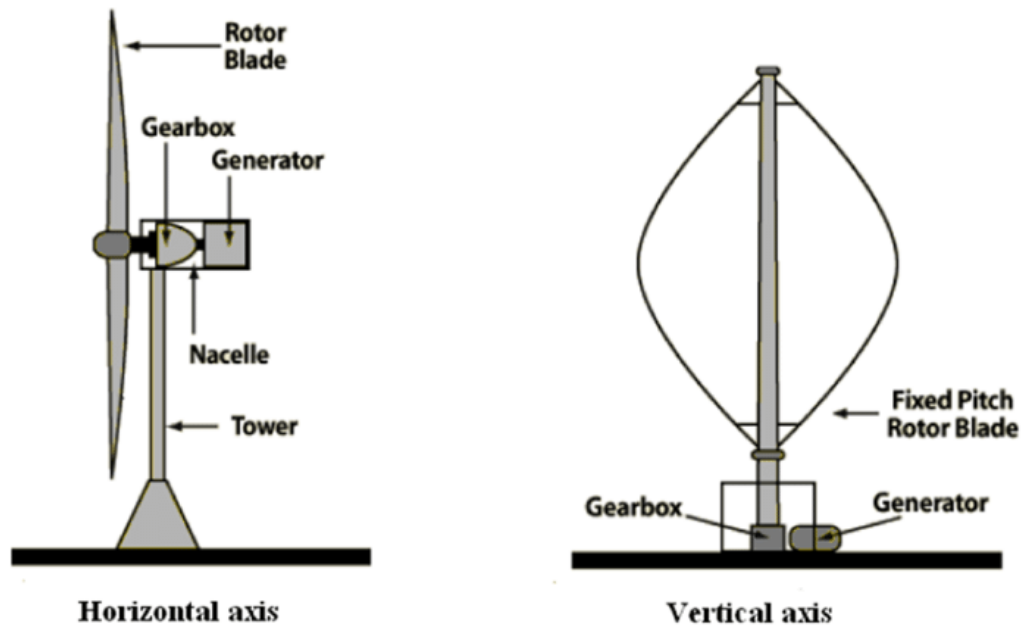
Figure 2: Comparison of Horizontal Wind Turbines to Vertical Wind Turbines [57]

Tension-Leg Platform Designs

Previous research in TLP designs started with single column designs [58]. Fulton et al. designed a multi-column floating platform utilizing a self-installing approach [59]. This platform was constructed using a three column spoke design attached to a center column through the use of connective tendons. Mooring cables are attached on the underside of each column providing stability on each of the corners and divides the forces evenly among the three separate columns. Suzuki et al. also based their research on this three column design for deployment off of Japans coast [60]. Two tendons were attached to each of the columns to provide even greater structural integrity. Another three column design was proposed by Zhao et al with the added factor of the hull structure being flexible [61]. After analyses completed over time, many designs have converged to the three column design. This not only allows the floating platform to keep the amount of material down, but with the added benefit of creating more surface area to decrease motion during wind and wave loading.
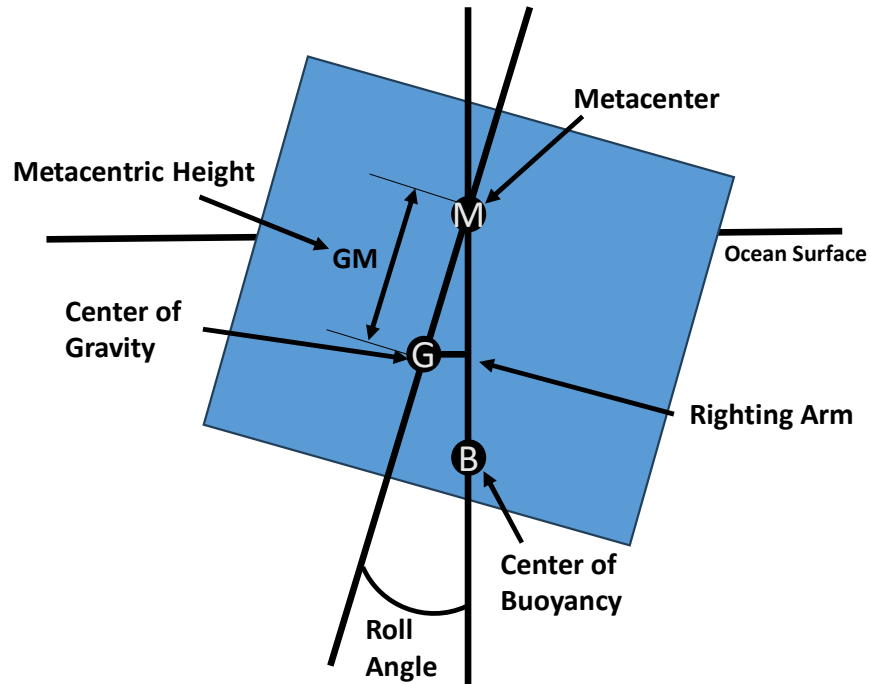
Figure 3: Metacentric Height Illustration [63]

Tension-Leg Platform Dynamics

Although TLPs have the shortest history when compared to other floating platform designs, much of the dynamics is shared among the many different designs and applications. Floating platforms also have a long and storied history with offshore oil platforms and a large portion of the dynamics from those interactions is also applicable in this instance since TLPs are constrained in place and often operate in a similar capacity to these older floating platforms [62].

Metacentric Height

Since these platforms are deployed in an aqueous body, the system needs to maintain hydrostatic stability to stay upright during the platform is towed and in operation [53]. As wind and wave loadings attack the floating platform, the tension in the mooring lines attempts to keep the body in place. The metacentric height requires calculations for the center of gravity and the buoyancy center. To ensure the setup remains upright, the metacentric height needs to remain

positive, but not too large. An excessively large metacentric height can adversely affect the floating platform and cause it to respond too stiffly to the incoming loading. Thus, we have to ensure our metacentric height remains in an acceptable range during design modification to keep our floating platform upright. A positive metacentric height means it remains above the surface of the water. By obtaining the center of gravity and the buoyancy center, we can ensure that this remains true throughout all of the design process. Figure 3 displays the metacentric height calculation, given as:

$$GM = KB + BM - KG \tag{1a}$$

$$BM = I_{\text{waterplane},xx}/\mathbb{V} \tag{1b}$$

$$GM = KB + I_{\text{waterplane},xx}/\mathbb{V} - KG \tag{1c}$$

where GM is the metacentric height, KB is the distance between keel (bottom of the submerged body) to center of buoyancy, BM is the distance between center of the buoyancy to metacenter, and KG is the distance between keel to center of gravity. BM is further calculated by taking division from the area moment of of inertia of the waterplane at the axis of rotation, $I_{\text{waterplane},xx}$, by volume of the submerged body, $\mathbb{V}$.

Mooring Lines

As mentioned previously, TLPs are secured in place connecting the floating platform to the anchoring point installed at the sea bed, which are commonly referred to as mooring lines. These mooring lines constrain the floating platform in place under tensile force during the entire operation of the floating platform. To achieve this, the platform is initially towed out to the deployment location with reusable flotation devices attached to the platform until the wind turbine is installed. The wires are then tensioned into place and the reusable flotation devices are removed. The tension in the mooring lines, weight of the platform and payload, along with the buoyancy force balances to each other on the whole platform, securing the platform body in

place. The mooring lines are designed to safely withstand cyclic loadings considering fatigue damages created by motions of the platform subject to probablistic metocean conditions over the design lifespan, typically around 25–30 years [12, 64].

Capytaine

Capytaine is an open-source linear potential flow boundary element method (BEM) solver used in obtaining required hydrodynamic coefficients in our study [65]. The code solves Laplace's differential equation in frequency domain to obtain velocity potentials on the boundary elements of the submerged body. The hydrodynamic forces in radiation and incident wave conditions can then be integrated over the discretized boundary elements. The details are given in the following chapter.

<center>Chapter 3</center>

<center>**Methodology**</center>

Overview

With offshore wind energy becoming a more acceptable and implementable source of renewable energy production, the design of the platforms used for deploying these turbines needs to be developed even further to keep up with the ever increasing demand placed on them by increasingly larger and more efficient designs for wind turbines. The topic of this research is the examination of a TLP to further iterate upon the design after previous research. To do this, an iterative optimization method is utilized to modify the outer hull of the floating platform and attempt to reduce the acceleration experienced in the Heave direction. TLPs naturally resist motion along the Surge and Sway directions so minimization of the Heave acceleration profile should provide the largest boost to resistance from incident wave loadings.

Finding the optimal solution requires us to setup the problem as an optimization problem. Doing this allows us to select specific portions of the floating platform that we would like to change and utilize them in the analysis. After the program is complete, the floating platform should result in a shape that combats the oncoming waves in such a way that the forces experienced in the Heave direction, are either reduced or dispersed into other DOFs.

Optimization problems can be solved in a number of various methods, but the current study uses the following problem in negative null form:

$$
\begin{aligned}
\underset{\mathbf{x}}{\text{minimize:}} \quad & \frac{1}{t_f - t_0} \sum_{k=1}^{6} C_{\text{scaling},k} \left(\int_{t_0}^{t_f} \dddot{\Xi}_k^2 \, dt \right)^{\frac{1}{2}} \\
\text{subject to:} \quad & A_{\text{outer-column}}(\mathbf{x}) - A_{\text{outer-column},0} = 0 \\
\text{subject to:} \quad & \sum_{t_0}^{t_f} (\Xi^2)^{1/2} = \sum_{t_0}^{t_f} (\Xi_0^2)^{1/2} \\
\text{where:} \quad & \dot{\Xi} - \mathbf{f}_d(\Xi, \mathbf{x}) = \mathbf{0},
\end{aligned}
$$

(2)

<center>12</center>

where C_{scaling} is a scaling factor applied to each DOFs seperately that ensures the objective function is not affected by round-off errors, t_0 (s) and t_f (s) are the initial and final times of the time-domain simulation, $\ddot{\Xi}$ (m/s^2) is the acceleration vector for all DOFs, $A_{\text{outer-column}}$ (m^2) is the cross-sectional area of the outer column and is a function of $\mathbf{x}$, $A_{\text{outer-column,0}}$ (m^2) is the cross-sectional area of the outer column at the baseline design ($\mathbf{x} = \mathbf{x}_0$), $\dot{\Xi}$ (m) is the velocity vector for all DOFs, and Ξ (m) is the displacement vector for all DOFs.

In this formulation, the objective function aims to minimize the sum of time-averaged platform accelerations across all 6-DOF directions. It is important to note that the acceleration values in each of the six DOFs have unique and significantly different scales. By summing the accelerations over these six DOFs, the optimizer is naturally encouraged to prioritize the design optimization with regard to DOFs characterized by larger scales, while still accounting for contributions from all directions. This approach ensures a balanced and effective optimization process that accounts for the varying impact of each DOF on the overall performance of the floating platform through the use of C_{scaling}.

Problem Definition

The acceleration profile for the floating platform can be obtained by modeling the system as a mass-spring-damper system. Dynamic interactions between the waves and the floating platform can be broken down and solved for the acceleration, velocity, and displacement profiles. Eq. (3) describes the simple mass-spring-damper system used.

$$M\ddot{\Xi} + D\dot{\Xi} + S\Xi = \sum \boldsymbol{F} \tag{3}$$

Here, M (kg) is the mass matrix for the floating platform, D (N-s/m) is the damping coefficient, S (N/m) is the stiffness matrix, and $\sum \boldsymbol{F}$ (N) is the force total experienced by the floating platform.

Each of these factors can be more fully defined and specified for the floating platform

shown in Eq. (4).

$$M\ddot{\Xi} + \int_0^t K(t - \tau)\dot{\Xi}(\tau)\,d\tau + (C + T)\Xi = \sum \boldsymbol{F} \tag{4}$$

The convolution integral in the second term on the left-hand side represents the hydrodynamic radiation-damping effect. In this convolution integral term, K represents the radiation-retardation kernel, which imparts the force with a memory effect from the structure's velocity-induced waves. C and T are the hydrostatic restoring coefficient and mooring line stiffness matrix respectively (N/m).

Now we can expand the sum of external forcesinto it's subsequent parts. This involves separating the sum into four distinct forces: Froude-Krylov force ($\boldsymbol{F}_{FK}$), Diffraction force ($\boldsymbol{F}_D$), and wind force ($\boldsymbol{F}_W$). We can also include the modified mass matrix by including the added mass parameter (A, kg). This adjustment creates a more accurate mass matrix as the floating platform drags water along during loading. Adding all this to our original equation gives us the following:

$$(M_{sys} + A_\infty)\ddot{\Xi} + \int_0^t K(t - \tau)\dot{\Xi}(\tau)\,d\tau + (C + T)\Xi = \boldsymbol{F}_{FK} + \boldsymbol{F}_D + \boldsymbol{F}_W \tag{5}$$

By solving the derivative of this equation, the acceleration and velocity profiles can be calculated and input into Eq. (5)

Initial Design

As mentioned previously, the bulk of research involving TLPs designs consist of floating platforms with a main center column with connective tendons attaching three outer columns to the center column. This design has been found to provide a high stability after full deployment. Mooring lines are attached to the underside of each of these outer columns and tensioned directly to the ocean floor. Pontoons are used for connective tendons that maintain structural rigidity. The inside of the frame is hollowed out to cut down on as much material as possible. This is also a large reason behind the three outer column design. An increasing number of outer columns have
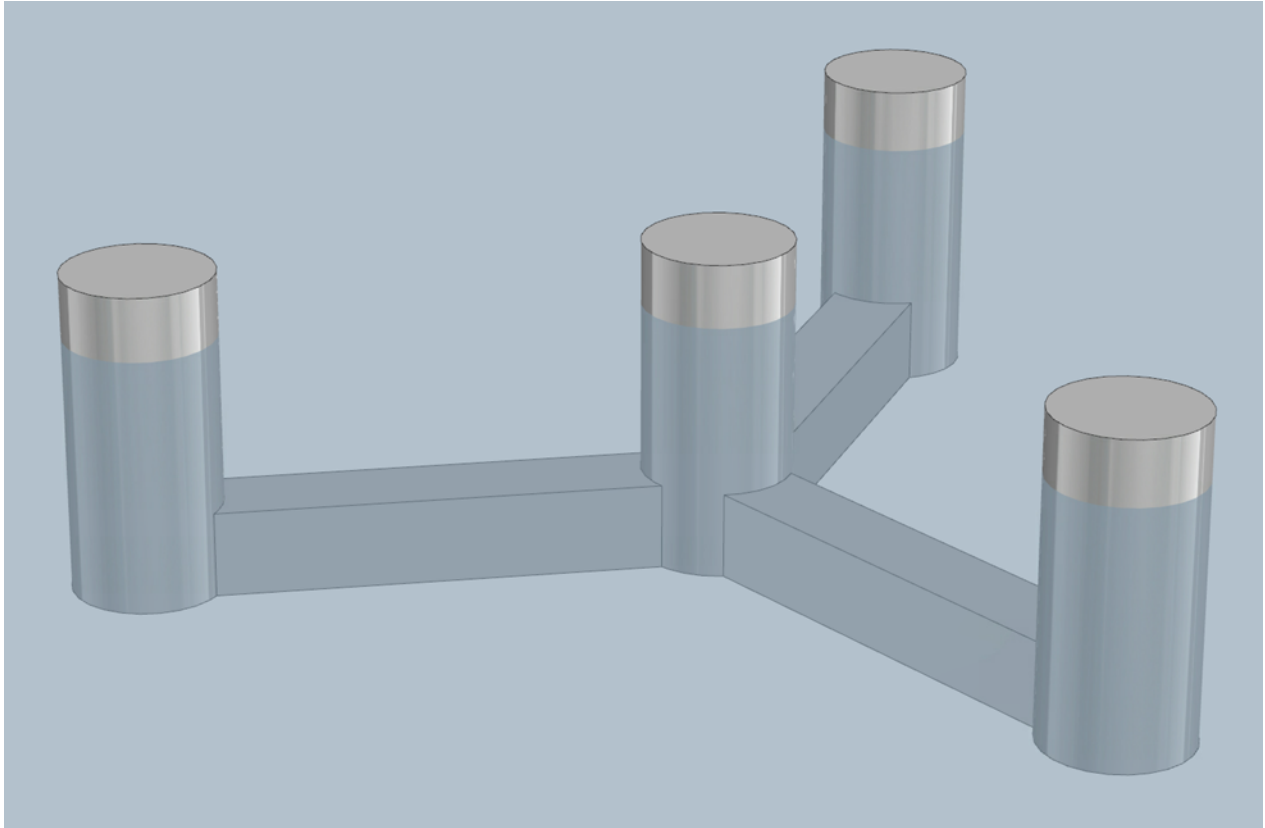
Figure 4: Three Column Tension Leg Platform (TLP) Design [66]

been analyzed such as four outer columns and five outer columns, but these designs require and equally increasing amount of material as well as increasingly complex moment arm mechanics. The original design used in this study, shown in the figure below, was first envisioned for research by Lee et. al and seen in Fig. 4. Their research provided the framework and a solid basis for the design moving forward and will be modified and attempted to be improved upon in this study.

Mesh

Another positive of this design is that it is easily transferred into a mesh. While Capytaine and many other software packages provide this ability in their core systems, for this model, we instead opted to create the mesh for the structure from the ground up [66]. The initial mesh was created by starting with the bottom of the floating platform shape, and lining that shape with
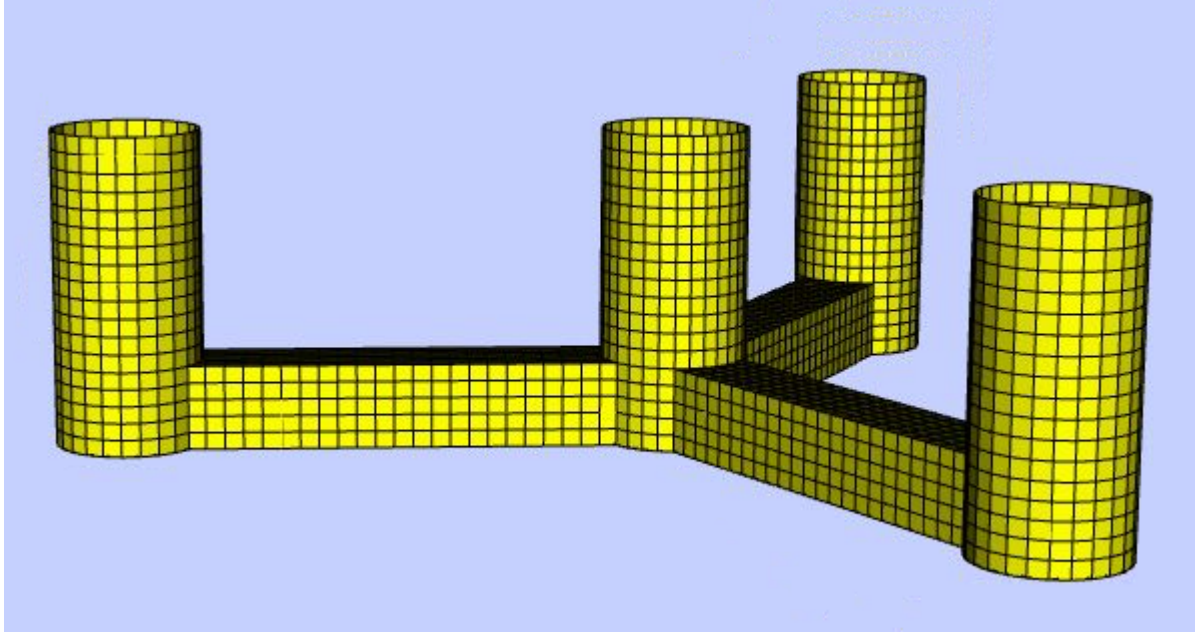
Figure 5: Meshed TLP Design [66]

points. The inside of the floating platform was filled out with points after this, with the pontoons being modeled completely parallel to each other and the center column and three outer columns being meshed circumferentially. The outer line of the mesh is then used to construct the rest of the floating platform until the desired height is reached. Upon completion, the meshed model in Fig. 5.

Mesh Analysis

Since the aim of this research is to optimize the shape of the chosen floating platform design, all calculations involving the meshed model need to be as accurate as possible. To this end, a mesh convergence test was performed on the model until an acceptable solution was found. This was defined as an increasingly small change between the Froude-Krylov forces produced from the calculations performed by Capytaine. The Tab. 1 outlines the number of mesh nodes present in each of the following data plots. There is a concern to have a increased error after making the mesh beyond certain density in the BEM solution of the linear Potential flow.

16

Table 1: Mesh Analysis Table

Case	Number of Nodes
M1	700
M2	1428
M3	1958
M4	2506
M5	3364
M6	3744
M7	3816
M8	4730
M9	5562
M10	6520
M11	6880
M12	7136
M13	7414
M14	7844
M15	8578
M16	8922
M17	9576

Thus, we included wide range of mesh density values in our analysis.

Figure 6 represents the Froude-Krylov energy by calculating the forces produced from Capytaine and integrating over the entire time frequency domain. These forces were obtained after calculation involving the various different mesh densities in the Surge, Heave, and Pitch DOFs. Increasing the number of nodes causes the system to follow a typical mesh analysis curve with diminishing returns occurring as the nodes increase past 3000 nodes. By using this, we can assume that using 3500 nodes will be accurate enough for the simulation when compared to using $10,000$ nodes.
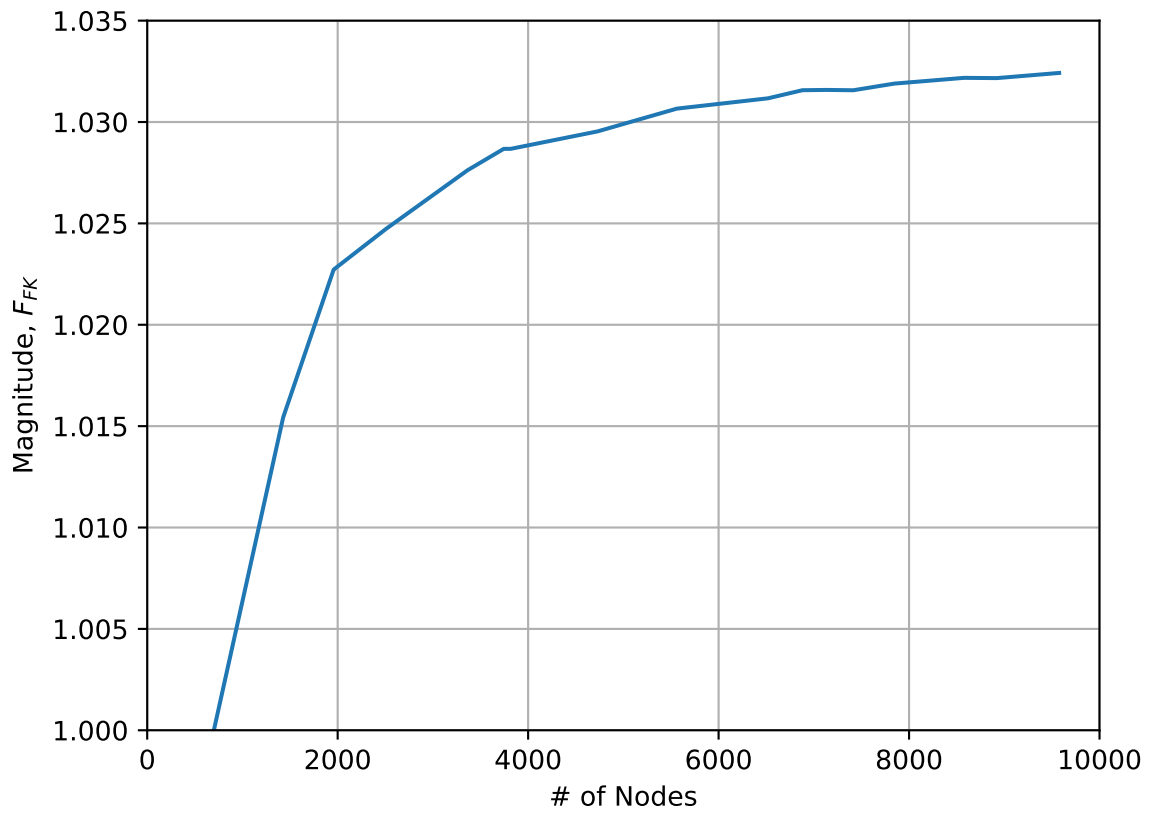
Figure 6: Froude-Krylov Energy vs. Mesh Nodes

Linear Potential Flow Wave Theory

For this calculation, it is assumed that the problem is linear. This makes the calculations much easier to work out and much easier to interface with Capytaine, which also assumes a linear problem. We can then write the Laplace equation as seen in Eq. (6), give as:

$$\nabla^2 \phi = 0 \tag{6}$$

where ϕ is the velocity potential defined as $u = \nabla\phi$ This problem can then be solved for in the frequency domain since it is linear. Equation (7) shows this transformation, given as:

$$\phi = \text{Re}(\Phi e^{-iwt}). \tag{7}$$

To solve this equation using the BEM method, we can solve the boundary integral problem using the Green function $G(\zeta, \cdot)$, which solves the partial differential equation, given as:

$$\nabla^2 G(x; \zeta) = \delta(\zeta - x) \tag{8}$$

where ∇ is meant as the derivative with respect to x. The Green function G allows us to solve for the potential of the surface of the floating body (Γ) by rewriting Eq. (8) as a function of a source distribution σ:

$$\Phi(x) = \iint_{\Gamma} \sigma(\zeta)G(x; \zeta)\, dS(\zeta) \tag{9}$$

for all points x in the fluid or on the hull of the floating body Γ. To calculate the integral on the surface of the hull, which is the main interest of this paper, the following formulation of Eq. (9), given as:

$$\frac{\partial \Phi}{\partial n}(x) = (u \cdot n)(x) = \frac{\sigma(x)}{2} + \iint_{\Gamma} x(\zeta)(\nabla G(x; \zeta) \cdot n)\, dS(\zeta) \tag{10}$$

where x is a point on Γ and n is the vector normal to Γ in x. For any vector t tangential to Γ at x, we have:

$$\frac{\partial \Phi}{\partial t}(x) = (u \cdot t)(x) = \frac{\sigma(x)}{2} + \iint_{\Gamma} x(\zeta)(\nabla G(x; \zeta) \cdot t) \, dS(\zeta) \tag{11}$$

Parameter Calculation

With the governing equation and the TLPs being defined, determination of the various parameters used in the calculations can be obtained.

Mass

One key component of the governing equation is the mass of the TLPs. Simple volumetric calculations are carried out to determine the platform mass as given in Tab. 2 and shown in Eq. (12), given as:

$$M = \rho \Psi \tag{12}$$

where ρ is the effective density of the material considering the density of the typical internal structures and Ψ is the volume of the material. We then use this simple calculation to obtain the full 6x6 mass matrix in Eq. (13), given as:

$$\mathbf{M} = \begin{bmatrix} M & 0 & 0 & 0 & M \cdot GC & 0 \\ 0 & M & 0 & -M \cdot GC & 0 & 0 \\ 0 & 0 & M & 0 & 0 & 0 \\ 0 & -M \cdot GC & 0 & I_{xx} & 0 & 0 \\ M \cdot GC & 0 & 0 & 0 & I_{yy} & 0 \\ 0 & 0 & 0 & 0 & 0 & Z_{zz} \end{bmatrix}. \tag{13}$$

where I_{xx}, I_{yy} and I_{zz} are the Moments of Inertia in the x, y and z directions and GC is the gravity center.

Table 2: Mass Analysis Table

Effective density (kg/m³)	Volume (m³)	Mass (kg)
294	4510	$1,326,900$

Moment of Inertia

To define the moment of inertia (I), we can start with the basic initial moment of inertia in the x, y and z directions:

$$I_{xx} = mR_{xx}^2, I_{yy} = mR_{yy}^2, I_{zz} = mR_{zz}^2 \tag{14}$$

where m is the mass of the system (kg) and R is the radius of the column (m). After that, we can iterate over the area of the object to derive the three dimensional moment of inertia equations. This is done as follows:

$$I_{xx,cc} = \int_{-H_{dr}}^{0} h^2 \mathbb{R}_{m,sm,cc}(A_{cc}, h)\, dh + \int_{0}^{H_{cc}-H_{dr}} h^2 \mathbb{R}_{m,fb,cc}(A_{cc})\, dh \tag{15a}$$

$$I_{xx,oc,fr} = \int_{-H_{dr}}^{0} h^2 \mathbb{R}_{m,sm,oc}(A_{oc}, h)\, dh + \int_{0}^{H_{oc}-H_{dr}} h^2 \mathbb{R}_{m,fb,oc}(A_{oc})\, dh \tag{15b}$$

$$I_{xx,oc,si} = \int_{-H_{dr}}^{0} (h^2 + L_{po}^2 \sin^2(\frac{\pi}{3}))\mathbb{R}_{m,sm,oc}(A_{oc}, h)\, dh$$
$$+ \int_{0}^{H_{oc}-H_{dr}} (h^2 + L_{po}^2 \sin^2(\frac{\pi}{3}))\mathbb{R}_{m,fb,oc}(A_{oc})\, dh \tag{15c}$$

$$I_{xx,po,fr} = \int_{-H_{dr}}^{-H_{dr}+H_{po}} h^2 \mathbb{R}_{m,po}(A_{po}, h)\, dh \tag{15d}$$

$$I_{xx,po,si} = \int_{-H_{dr}}^{-H_{dr}+H_{po}} (h^2 + (\frac{2L_{po} + D_{cc} - D_{oc}}{4}\sin(\frac{\pi}{3}))^2)\mathbb{R}_{m,po}(A_{po}, h)\, dh \tag{15e}$$

$$I_{yy,cc,fr} = \int_{-H_{dr}}^{0} h^2 \mathbb{R}_{m,sm,cc}(A_{cc}, h)\, dh + \int_{0}^{H_{cc}-H_{dr}} h^2 \mathbb{R}_{m,fb,cc}(A_{cc})\, dh \tag{15f}$$

$$I_{yy,oc,fr} = \int_{-H_{dr}}^{0} (h^2 + L_{po}^2)\mathbb{R}_{m,sm,oc}(A_{oc}, h)\, dh + \int_{0}^{H_{oc}-H_{dr}} (h^2 + L_{po}^2)\mathbb{R}_{m,fb,oc}(A_{oc})\, dh \tag{15g}$$

$$I_{yy,oc,si} = \int_{-H_{dr}}^{0} (h^2 + L_{po}^2 \cos^2(\frac{\pi}{3})) \mathbb{R}_{m,sm,oc}(A_{oc}, h) \, dh$$

$$+ \int_{0}^{H_{oc}-H_{dr}} (h^2 + L_{po}^2 \cos^2(\frac{\pi}{3})) \mathbb{R}_{m,fb,oc}(A_{oc}) \, dh \tag{15h}$$

$$I_{yy,po,fr} = \int_{-H_{dr}}^{-H_{dr}+H_{po}} (h^2 + (\frac{2L_{po} + D_{cc} - D_{oc}}{4})^2) \mathbb{R}_{m,po}(A_{po}, h) \, dh \tag{15i}$$

$$I_{yy,po,si} = \int_{-H_{dr}}^{-H_{dr}+H_{po}} (h^2 + (\frac{2L_{po} + D_{cc} - D_{oc}}{4} \cos(\frac{\pi}{3}))^2) \mathbb{R}_{m,po}(A_{po}, h) \, dh \tag{15j}$$

$$I_{zz,cc} = 0.5(m_{sm,cc} + m_{fb,cc}) \frac{D_{cc}^2}{4} \tag{15k}$$

$$I_{zz,oc} = (m_{sm,oc} + m_{fb,oc}) L_{po}^2 \tag{15l}$$

$$I_{zz,po} = m_{po}(\frac{2L_{po} + D_{cc} - D_{oc}}{4})^2 \tag{15m}$$

where h is the height at a certain point of the integral, H is the total height of the object (m), L is the length (m), D is the diameter (m), cc is the subscript denoting the center column, oc is the subscript deonting the outer columns, po is the subscript denoting the pontoons, fr is the subscript denoting front, si is the subscript denoting side, fb is the subscript denoting freeboard, sm is the subscript denoting submerged, dr is the subscript denoting draft, and $\mathbb{R}$ represents the empirical regression function.

Center of Gravity

The gravity center is important for the metacentric height calculations as well but is calculated separately from the moment of inertia. Gravity centers for x and y can be equated to 0 since the structure is completely symmetrical:

$$GC_{xx} = GC_{yy} = 0 \tag{16}$$

We can add up the total mass of the system to calculate this by summing the total mass of the three outer columns, the center column, and all three pontoons, given as:

$$m = m_{sm,cc} + m_{fb,cc} + 3m_{sm,oc} + 3m_{fb,oc} + 3m_{po} \tag{17}$$

The gravity center in the z direction can be found by summing the total gravity centers of the system, given as:

$$GC_z = \frac{\left[\begin{array}{l} m_{sm,cc}GC_{sm,cc} + m_{fb,cc}GC_{fb,cc} + 3m_{sm,oc}GC_{sm,oc} \\ +3m_{fb,oc}GC_{fb,oc} + 3m_{po}GC_{po} \end{array} \right]}{m} \tag{18}$$

Each of the separate gravity centers can be found by integrating the area of the object and dividing by its mass which can be calculated as follows:

$$GC_{sm,cc} = \frac{1}{m_{sm,cc}} \int_{-H_{dr}}^{0} h \mathbb{R}_{m,sm,cc}(A_{cc}, h) \, dh \tag{19a}$$

$$GC_{fb,cc} = \frac{1}{m_{fb,cc}} \frac{(H_{cc} - H_{dr})^2}{2} \mathbb{R}_{m,fb,cc}(A_{cc}) \tag{19b}$$

$$GC_{fb,oc} = \frac{1}{m_{sm,oc}} \int_{-H_{dr}}^{0} h \mathbb{R}_{m,sm,oc}(A_{oc}, h) \, dh \tag{19c}$$

$$GC_{fb,oc} = \frac{1}{m_{fb,oc}} \frac{(H_{oc} - H_{dr})^2}{2} \mathbb{R}_{m,fb,oc}(A_{oc}) \tag{19d}$$

$$GC_{po} = \frac{1}{m_{po}} \int_{-H_{dr}}^{-H_{dr}+H_{po}} h \mathbb{R}_{m,po}(A_{po}, h) \, dh \tag{19e}$$

Hydrostatics

The hydrostatic stiffness refers to the forces exerted on a submerged body due to hydrostatic pressure, which act to restore the body's orientation when it is displaced from its equilibrium position. These forces counteract the effects of both hydrostatic and gravitational forces to maintain the body's stability and equilibrium while submerged. Hydrostatic stiffness
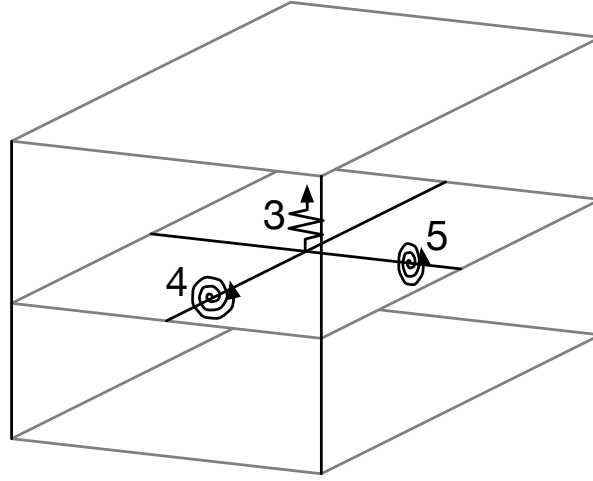
Figure 7: Hydrostatic stiffness DOFs

can be obtained by computing the integral shown in Eq. (20), give as:

$$C_{ij} = \rho g \iint_S (\hat{n} \cdot V_j)(w_i)\, dS \tag{20}$$

where $\hat{n}$ is the surface normal and $V_i = u_i \hat{n}_x + v_i \hat{n}_y + w_i \hat{n}_z$ is the DOF vector. This exact formula can only be calculated while using rigid body DOFs. Since the restoration forces are all related to DOFs 3 (heave), 4 (roll), and 5 (pitch), the completed hydrostatic stiffness matrix has 9 components, namely C_{ij} where $i = 3, 4, 5$ and $j = 3, 4, 5$.

Since the hydrostatic stiffness and the mooring lines directly impact each other, it is important for us to specify the specifics of the mooring cables used. There are many different variations on the model, but the tension leg design shown in Fig. 8 After careful research and consideration, the following value for mooring line tension was chosen to match all requirements along with the specified length. Here, T is the tension in the lines due to the gravitational weight combined with the buoyancy force of the floating platform, S is the stiffness in the lines, L is the length of the lines, and F is the fairlead depth. Table 3 shows the input parameters for this study.

Table 3: Mooring Line Parameters

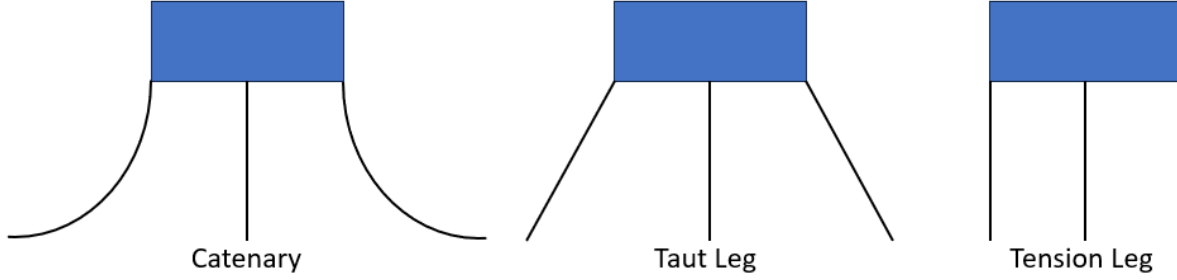| Stiffness (N/m)	Length (m)	Fairlead Depth (m)
2.11×10^9	80.0	15.0

Figure 8: Mooring Line Variations [59]

These values were then compiled into a mooring matrix to accurately represent the stiffness for the system in all DOFs. Equation (21) displays this matrix in full form.

$$\mathbf{ML} = \begin{bmatrix} \frac{3T}{L} & 0 & 0 & 0 & -\frac{3T*F}{L} & 0 \\ 0 & \frac{3T}{L} & 0 & \frac{3T*F}{L} & 0 & 0 \\ 0 & 0 & \frac{3T}{L} & 0 & 0 & 0 \\ 0 & \frac{3T*F}{L} & 0 & \frac{3T\cdot F^2}{L} + \frac{0.5S}{L\cdot F^2} + T\cdot F & 0 & 0 \\ -\frac{3T*F}{L} & 0 & 0 & 0 & \frac{3T\cdot F^2}{L} + \frac{0.5S}{L\cdot F^2} + T\cdot F & 0 \\ 0 & 0 & 0 & 0 & 0 & \frac{nT\cdot F^2}{L} \end{bmatrix} \quad (21)$$

Hydrodynamics

Along with the hydrostatics of the system, the hydrodynamics of the TLP need to be analyzed to complete the problem definition. This is done in two parts where both are completed in the frequency domain. The first is analysis of the radiation problem where we can obtain the

added mass and radiation damping coefficient. Second is the diffraction problem where the Froude-Krylov and diffraction forces are obtained. The radiation problem is solved for each radiating 6DOFs and calculated along the influenced 6DOFs. The diffraction problem is solved to calculate the excitation forces in 6DOFs to obtain the forcing terms.

Added mass is equivalent to the amount of volume of fluid being displaced during motion of the floating platform. This is due to the platform imparting some energy into the fluid and attempting to break free from it. This results in an added mass matrix that is $6x6$DOF to match the initial mass matrix. Combining these gives the fully completed mass matrix.

Both diffraction problems and radiation problems are solved by integrating the pressure field over the entire floating body. The radiation damping forces acting on the body's surface are due to the interaction between specified radiating DOFs and the influenced DOFs. The diffraction forces are calculated from the integration of the diffracted wave field with the floating body remaining fixed. Froude-Krylov forces are calculated through integration of the incident wave field pressure created by incoming plane waves.

Convolution Integral

Since the present solution is represented in the frequency domain, the present solution must be transformed back into the time domain to calculate the acceleration, velocity and displacement profiles. Solving for the external forces requires use of the convolution integral. After that is solved, the forces are represented in the time domain and used in the time domain integration.

Problem Solution

Now that the constituent pieces have been assembled, the acceleration and velocity profiles can be obtained through time domain integration. This can be done by taking the force total at the current time step and subtracting the force total from the previous step. Our mass matrix is then inverted and multiplied on the other side to result in the acceleration profile. We

Table 4: Brief Summary of the Capytaine Inputs

Frequency (ω)	0.5 rad/s	1.0 rad/s	
Wave Direction	0 rad		
Radiating DOF	Surge	Roll	Pitch
Water Depth	100.0 m		
Time	60 s		
Time Step	0.02 s		

can then substitute this profile back into the previous equation resulting in our displacement profile.

Inputs

Wave and wind loadings out in nature are incredibly stochastic in nature. Computers, however, are simply incapable of replicating this stocasticity. That is not to say that it is impossible to recreate the loading however. With careful consideration for the input parameters, a size-able amount of the loadings can be replicated for the loadings that would be experienced by the floating platform during normal operation. To this end the following input parameters were utilized:

Frequency

For the frequency (in angular velocity, ω rad/s) selection, two separate values were chosen: 0.5 and 1.0 rad/s. This selection was motivated by several factors, primarily for reducing computational time. With each simulation taking days or even weeks, it was imperative to maximize the efficiency of the system and cut down on as much computation time as possible. To do this, originally, a much wider range of frequency values were chosen increasing from the original 0.1 rad/s to 5.0 rad/s and an even higher 10.0 rad/s. After careful observation of the resulting analysis, the added number of frequency values did not result in a significantly better solution. Thus, these larger values were cut in an attempt to reduce the overall computation time

by a significant margin while not reducing the overall accuracy of the ending results. Analysis of real life wave loadings show that the majority of wave loadings exist in the 0.5 to 1.0 rad/s range, adding further credibility to the choice to omit the larger frequency values [67].

These two values define a simple scenario in which several waves appear over the given time frame. One wave per second is a reasonable approximation to real life stochastic loading since the majority of ocean currents operate on a wave loading roughly once every second. Not only does this add even more credence to leaving out higher values for frequency, it also shows that our approximation is closer to the average wave loading experienced than if the other much higher frequency values were chosen.

Wave Direction

For wave direction, there were many options to consider, but ultimately, a straight forward approach of using 0 radians was deemed acceptable [67]. With the common application of these wind turbines, predictable paths for water current flow and typical wind directional flow are more commonly known. Current paths have been extensively mapped out and are still continually being developed to better understand offshore movements. offshore wind patterns are also more recognizable with the large amount of research necessary before deployment of these offshore wind turbines. Thus, it is acceptable to assume that the application in which the TLP is placed will result in the most straightforward approach to maximize wind energy transfer efficiency.

Radiating Degrees of Freedom

For our radiating DOFs, the chosen directions were Surge, Roll, and Pitch. These directions denote movement of the floater as it is pushed on by the incoming waves as well as the rotational movement generated by the waves about the central axis of the floating platform. Radiation in the Surge direction correlates to a wave direction of 0 rad which was the wave direction chosen for this study. Roll and Pitch also correlate to rotational movement about the Surge axis, creating slight motions in both the Sway and Heave directions as a response. This

28

helps alleviate the need for added radiating DOFs in addition to creating a more realistic wave profile loading for the simulation and resulting calculations.

As the waves attack the floating platform, the water level rises in response to the amplitude of the wave, thus moving the platform up and down without the need for specification of radiation in the Heave direction. The same method applies for Sway except the reason for Sway being omitted from the radiating DOFs is that the wave loading is, again, applied in the direction perpendicular to the from face of the floating platform. This means that any translational motion along the Sway direction will be due to motion induced in the Heave direction causing it to not be a necessary inclusion in the calculations.

Infinite Response Problem

There is one more very specific case that needs to be added to the calculations in order to provide an accurate simulation of the problem. As mentioned previously, the mass of the system is not only comprised of the mass of the floating platform and the turbine components, but also the amount of mass of water that is dragged around with the floating platform in response to the wave loading. This mass is represented as the added mass of the system and is vital for calculations involving the acceleration profile of the floating platform.

To determine this added mass, the radiation problem needs to be solved at an infinite response frequency, or $\omega \rightarrow \infty$ rad/s. This correlates to an infinite amount of waves impacting the floating platform per second. Not only does this provide the most extreme case, it also provides the most accurate added mass for the system since it is attempting to push an infinite amount of water past the platform per second causing it to have the largest amount of mass being pushed around with the floating platform. Using this, we can more accurately construct our mass matrix and calculate a more accurate acceleration profile for the floating platform.

It is also important to validate the adequacy of time step, set at 0.002 s, for resolving the problem in time marching simulation. This verification involves a time advancement simulation of the dynamic problem with a simple circular shaped geometry. The determination entails

calculating the total displacement and velocity of the system in all DOFs by integrating the velocity or acceleration vector of the platform over the entire time span. The results, as presented in Fig. 9, reveal that increasing the time step size over 0.01 s rapidly increases the error in the solution. The difference in results between 0.001 s and 0.002 s is relatively smaller when compared to the total solution. Consequently, the utilization of a time step of 0.002 s was deemed adequate for the time domain accuracy in the simulation.

Floating Platform Design Optimization

This study is interested in the optimization of the floating platform through changes incurred in the outer hull shape and the responding acceleration profile. Because the outer shape is defined by a mesh lining the outer wall and the outer columns are meshed circumferentially, our focus will be on adjusting the outer nodes on the three outer columns and running the model through the simulation repeatedly until the most optimal shape is reached. Due to the mesh being created in this way, each of the three outer columns is created identically to the others. We can use this to our advantage in the design by choosing multiple points along the outer shape and choosing them to be the basis for the design optimization. By doing this, we can contort the mesh circumferentially along the outer column shapes and gain the desired shape without excessive modification to the mesh. We can also define several points on the inside of the outer columns to ensure rigid connection to the pontoons connecting the platform. These pontoons provide a large portion of the structural rigidity of the system so keeping their attachment as rigid as possible will prove vital in ensuring the design remains structurally sound even after excessive modifications. Seven nodes were selected on the outside columns of the floating platform and five nodes were constrained near the pontoons to ensure rigidity while also allowing for dynamic modification of the structure.
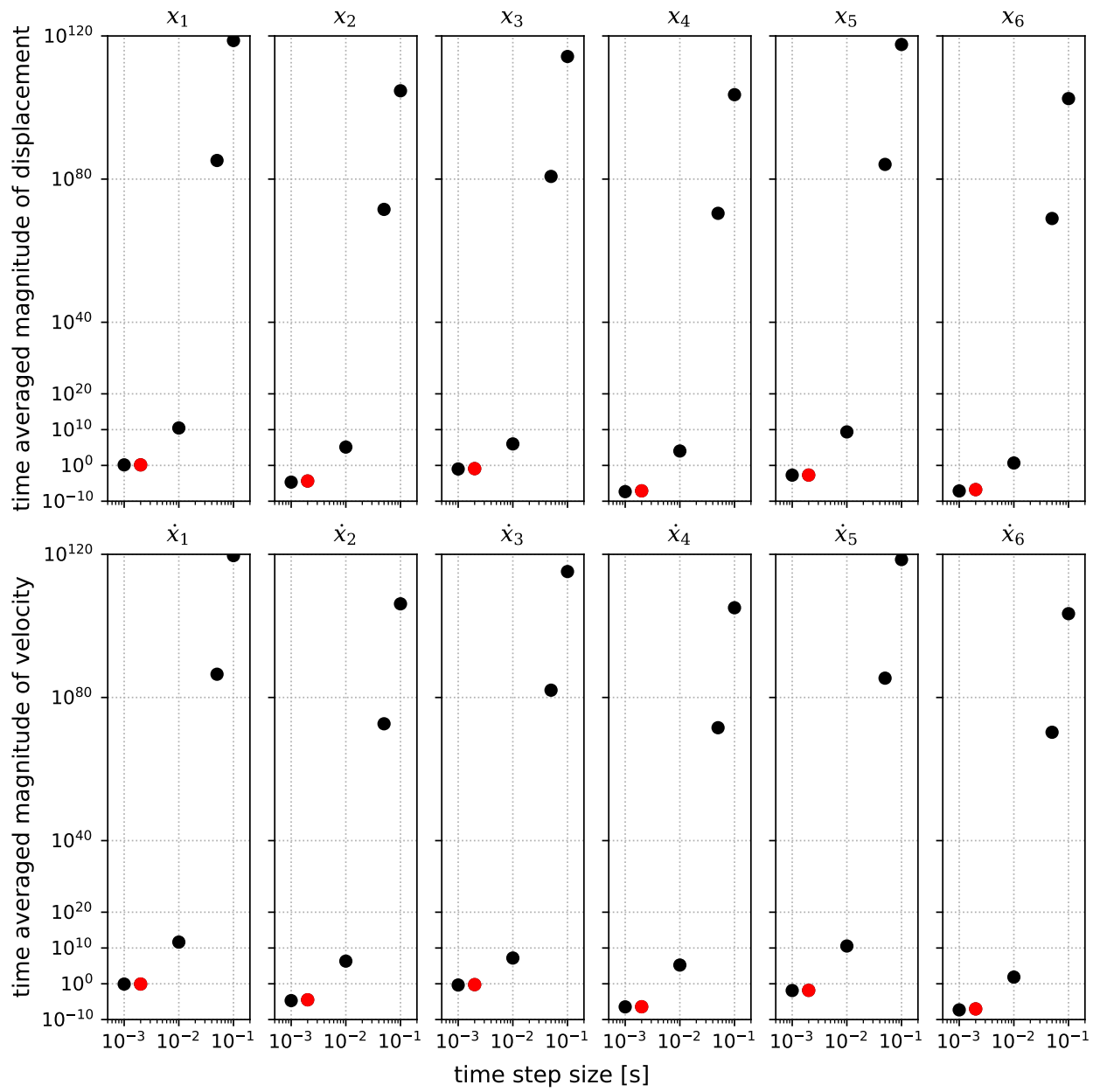
Figure 9: Time Step Size Study

Chapter 4

Results and Discussion

Initial calculations for the TLP were done on the base design outlined in Chap. 3. Results from these calculations were used as the basis for the constraints of the floating platform in the optimization method. Along with this, two arbitrarily chosen shapes were analyzed alongside the initial shape to analyze the design space. These shapes violated the area constraint but presented different geometries that can be seen in Fig. 10. The results from these simulations can be seen in the Tab. 5. These shapes overall performed significantly worse than the original design, increasing the heave acceleration. Because the shapes were designed manually using intuition, the area was not kept constant, but similar to the original. After analysis, it was clear that the increase in area caused an increase in all DOFs motions. The pointed shape also caused the water to divert from the outer columns and attack the center column, increasing stress on the floater overall.

Optimization of the TLP was performed a number of times from various starting positions until the max allowable iterations were completed or convergence was found. A summary of these shapes and results are shown in Tab. 5. Figures 11 and 12 showcase the system displacement and acceleration trajectories in the surge, heave, and pitch DOFs for the Analysis 1, 2, 3 and the Optim 2 cases.

When compared to the baseline case (Analysis 1), the arbitrary irregular shapes utilized in the Analysis 2 and 3 cases demonstrate higher amplitudes in both displacement and acceleration trajectories across all DOFs. However, the optimized solution provided by the Optim 2 case exhibits notably reduced amplitudes in both displacement and acceleration trajectories for the heave DOF motion, albeit at the expense of slight increase in the amplitudes of the pitch DOF motion.

Figures 13 and 14 depict the time-averaged displacement and acceleration magnitudes within the surge, heave, and pitch DOFs for the instances of Analysis 1, 2, 3 and the Optim 2

Table 5: Analysis and Optimization Cases, Initial Conditions, and Solutions

	Initial condition	Numerical solution	
Case	Shape and radius	Objective function	Constraint violation
Analysis 1	Circular, 3.5 m (Baseline)	1.374377	0.000×10^0
Analysis 2	Irregular #1	1.402011	1.564×10^0
Analysis 3	Irregular #2	1.473139	6.281×10^0
Optim 1	Circular, 3.5 m (Baseline)	1.316513	5.332×10^{-3}
Optim 2	Circular, 3.4 m	1.313484	2.194×10^{-4}
Optim 3	Circular, 3.8 m	1.320251	2.499×10^{-4}
Optim 4	Irregular #1	1.331540	2.549×10^{-4}

cases. The bar graphs are normalized to the results of the baseline case. Thus, the baseline case

magnitudes are 1.0 for all DOFs. These figures clearly displays the average magnitude relative

to the baseline case. Arbitrarily-created irregular shapes (Analysis 2 and 3) exhibit inferior

performances in all DOFs in terms of both displacement and acceleration. However, Optim 2

result exhibit a significantly reduced displacement and acceleration in the heave DOF, with a

slightly increased acceleration in the pitch DOF, as we discussed above.

Figure 15 shows the optimal cross-sectional shapes of the outer column for the Optim 1-4

cases, contrasting them with the baseline design (Analysis 1). Although the objective function

values for all four cases are remarkably similar, optimal solutions in terms of the cross-sectional

shapes exhibit notably different designs. However, it is evident that the optimal solutions tend

to converge toward concave shapes at the outermost location of the platform. Generally, longer

pontoons are more susceptible to wave loadings, but they also offer improved hydrodynamic

rigidity at the same time. Nonetheless, considering the relatively smaller pitching DOF motion in
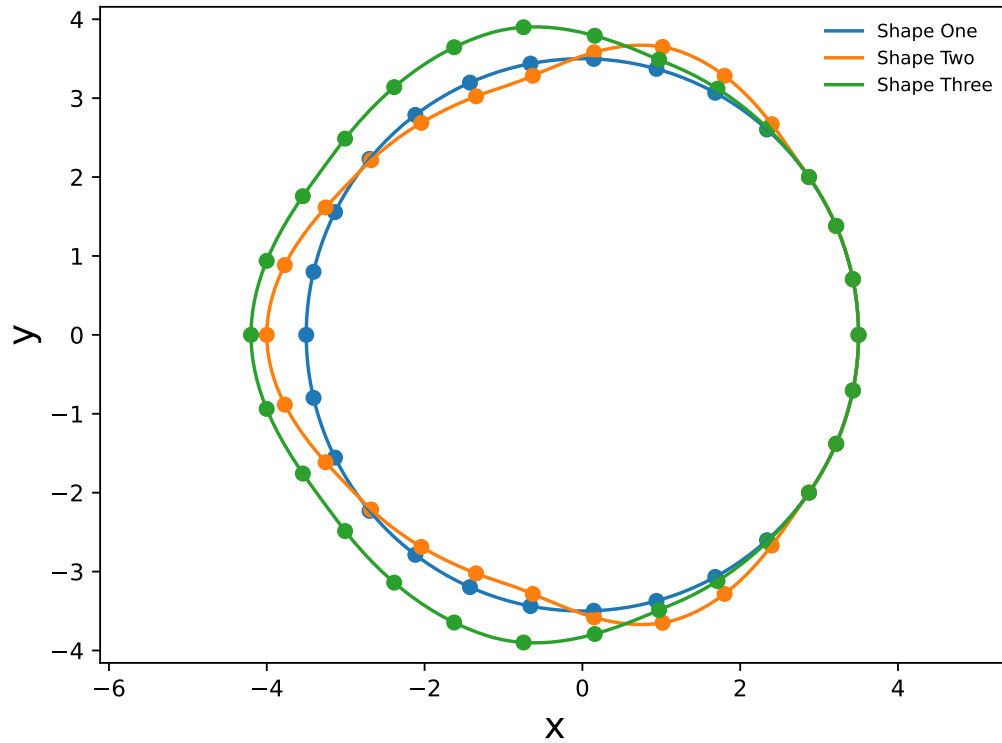
Figure 10: Varied (Circular and Irregular) Cross-Sectional Shapes of the Outer Column

comparison to other two major DOFs due to the characteristics of the TLP, one can hypothesize that the concave and wider outer column shapes may effectively provide benefits similar to those offered by a shorter pontoon design.

Optim 2 showed the most significant performance out of the optimization runs and was thus chosen for further study into the cause of the indented heart-like shape. Figures 16 through 23 show the panel meshes for the original circular design and the indented heart design and the visualized pressure field due to incoming waves on the body in surge and heave DOFs.

With the meshes being changed and distorted during analysis, we can take a closeup view of the Optim 2 mesh compared to the original circular floater shape shown in Fig. 18 and a closeup view in Fig. 24. The two meshes display significant distortion of the outer nodes of the mesh, squashing in the triangular nodes on the outer edge. Our primary focus does not involve calculating shear stress of the fluid element; therefore, abrupt changes in mesh size do not raise immediate concerns. Our approach involves surface integration within each boundary element

cell, making highly skewed elements undesirable. Nonetheless, despite some distortion in certain squares within the mesh's interior, they maintain a reasonable skewness considering the overall shape. While the triangular elements largely retain their shape within acceptable skewness limits, some squares exhibit a relatively greater level of distortion, albeit within reasonable limits. Given that the meshing software was originally tailored for circular columns, employing a more versatile meshing software could result in a more consistent mesh compared to what we obtained in this study.

From the models, we can see that the pressure field in the heave direction for the optimized design is indeed lighter than that seen on the original design. This appears to be due to the increase in distance from the center for a large majority of the heart shape with the outer sections providing increased reduction to the overall pressure field. We can also see a slight increase in the pressure on the outer columns and a decrease in pressure on the center column in Fig. 22(b). Even though the heart shaped design on the outer columns is absorbing much more of the impact from the waves approaching the floating platform, it is reducing the overall pressure and hence force on the center column. Earlier analysis showed confusing results with the heart shape due to it being a stagnation point for water, and theoretically increasing the forces experienced by the TLP, but this had the unforeseen effect of reducing loading on the center column, likely due to the outer column taking more of the force. The outer columns can endure much more of the load than the center column of the structure due to the mooring lines being attached at this point, but the center column relieves the forces through bending of the central tower. Not only does the optimized shape reduce the overall heave motion of the floating platform, but it simultaneously relieves some stress from the most critical part of the platform and redistributes it among the outer columns.

To further analyze the changes in acceleration caused by the floating platform, we can look to the added mass of the system since it plays such a vital role in direct calculation of the acceleration profile. Equations (22a) and (22b) display the added mass matrices for the original

35

circular floating platform design and the heart shaped optimal design, respectively, given as:

$$
\mathbf{A}_1 =
\begin{bmatrix}
2.865\text{e}+06 & -2.700\text{e}-10 & -6.693\text{e}+01 & -3.183\text{e}-09 & -2.103\text{e}+07 & -8.731\text{e}-08 \\
-4.547\text{e}-10 & 2.865\text{e}+06 & 2.416\text{e}-10 & 2.103\text{e}+07 & 9.095\text{e}-10 & -1.610\text{e}+03 \\
5.178\text{e}+01 & 1.990\text{e}-10 & 1.595\text{e}+06 & 3.092\text{e}-08 & -1.473\text{e}+03 & 3.183\text{e}-09 \\
-2.728\text{e}-09 & 2.108\text{e}+07 & 3.183\text{e}-08 & 4.073\text{e}+08 & 3.456\text{e}-08 & -8.107\text{e}+04 \\
-2.108\text{e}+07 & 4.547\text{e}-10 & -4.788\text{e}+02 & 2.547\text{e}-08 & 4.072\text{e}+08 & 5.821\text{e}-07 \\
-9.823\text{e}-08 & -1.491\text{e}+02 & 2.842\text{e}-10 & 6.750\text{e}+04 & 5.821\text{e}-07 & 1.695\text{e}+09
\end{bmatrix}
\tag{22a}
$$

$$
\mathbf{A}_2 =
\begin{bmatrix}
3.136\text{e}+06 & 6.915\text{e}-01 & -7.829\text{e}+01 & -2.183\text{e}+00 & -2.255\text{e}+07 & -3.127\text{e}-01 \\
-7.136\text{e}-01 & 3.136\text{e}+06 & 2.265\text{e}-03 & 2.256\text{e}+07 & -1.912\text{e}+00 & 1.345\text{e}+02 \\
4.738\text{e}+01 & -8.790\text{e}-02 & 1.582\text{e}+06 & -6.563\text{e}-01 & -1.347\text{e}+03 & -1.338\text{e}+01 \\
-1.175\text{e}+01 & 2.256\text{e}+07 & 2.715\text{e}-01 & 4.130\text{e}+08 & 4.689\text{e}+01 & -3.962\text{e}+04 \\
-2.256\text{e}+07 & -1.007\text{e}+01 & -2.029\text{e}+02 & -3.523\text{e}+01 & 4.129\text{e}+08 & 1.555\text{e}+01 \\
-2.417\text{e}-01 & 3.398\text{e}+03 & -1.676\text{e}+01 & 8.961\text{e}+04 & 1.538\text{e}+00 & 1.890\text{e}+09
\end{bmatrix}
\tag{22b}
$$

By looking at the diagonal terms from elements $A_{1,11}$ to $A_{1,33}$ from Eq. (22a) and from $A_{2,11}$ to $A_{2,33}$ from Eq. (22b), increased values in added mass directly affect as significant increased moment of inertia values of the body in surge (11) and sway (22) DOFs, with minimal decrease in heave (33) DOF. Furthermore, diagonal terms from elements $A_{1,44}$ to $A_{1,66}$ from Eq. (22a) and from $A_{2,44}$ to $A_{2,66}$ from Eq. (22b) shows the increased values in added mass, directly affecting rotational DOFs of the body in roll (44), pitch (55), and yaw (66) directions. These clues suggest that we can understand improved stability in accelerations subject to the same amplitude and profile of incident wave in the way that overall increased mass has caused less overall motion due to effectively larger moment of inertia experienced by the hydrodynamic interactions.
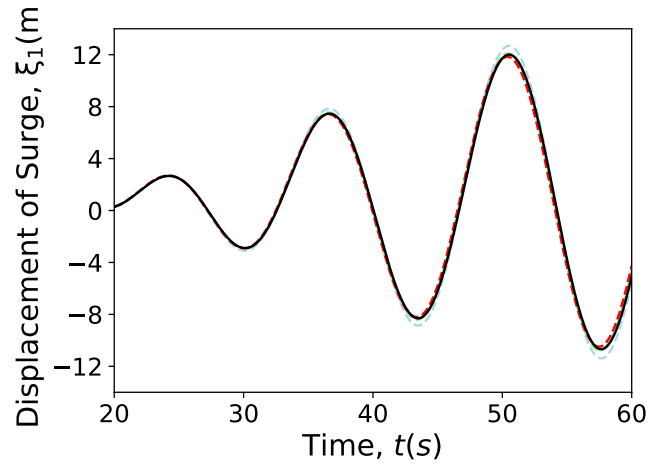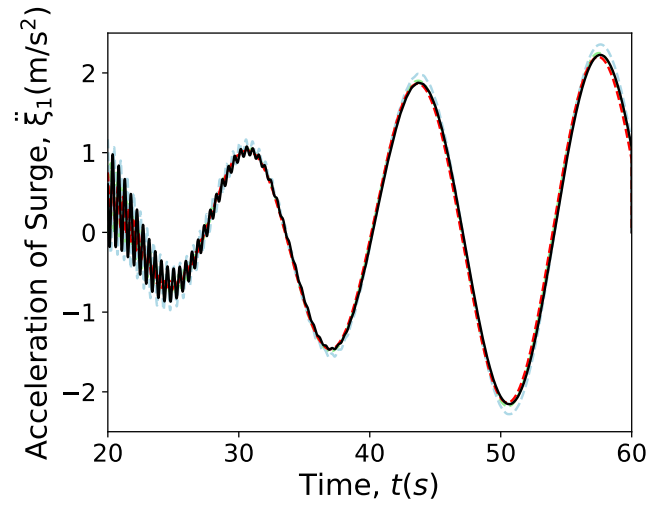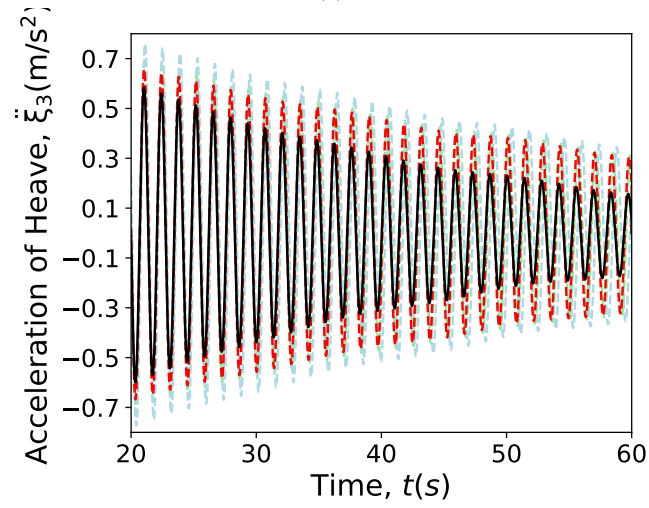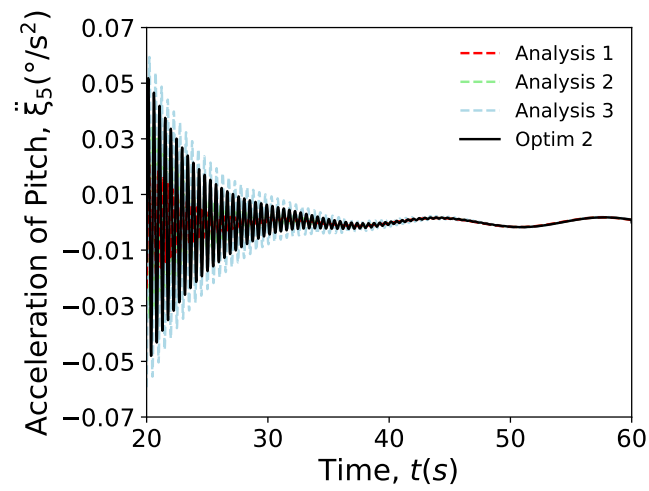
(a)
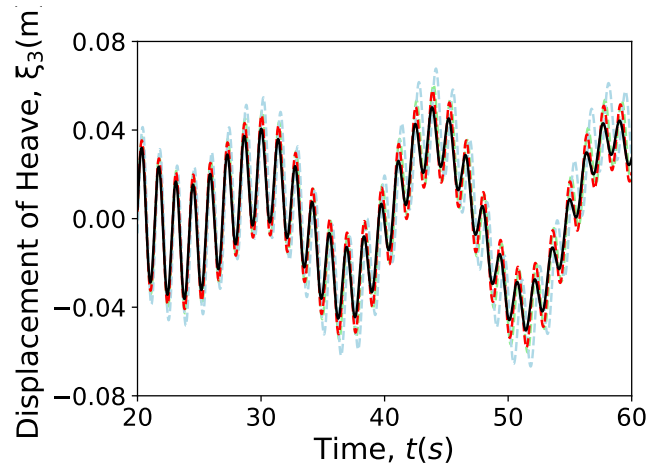
(b)
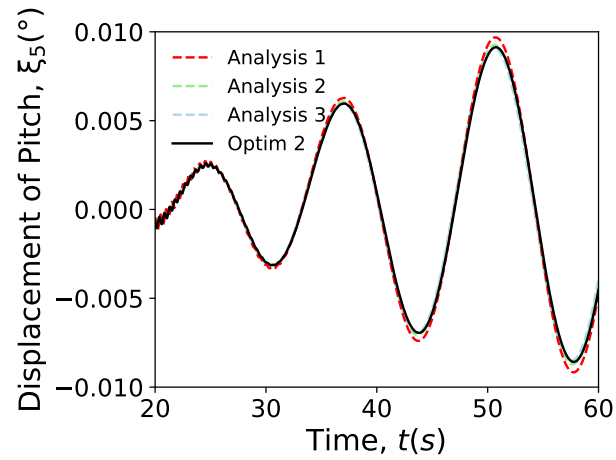
(c)

Figure 11: Displacement of Floating Platforms With Varied Designs

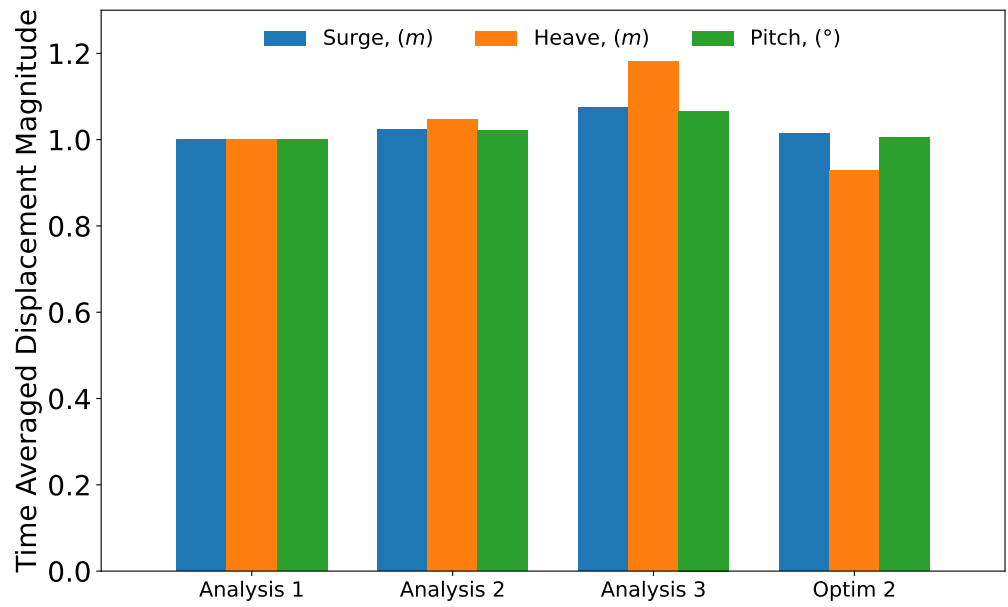Figure 12: Acceleration of Floating Platforms With Varied Designs

Figure 13: Time-Averaged and Normalized Displacements for Floating Body Surge, Heave, and Pitch
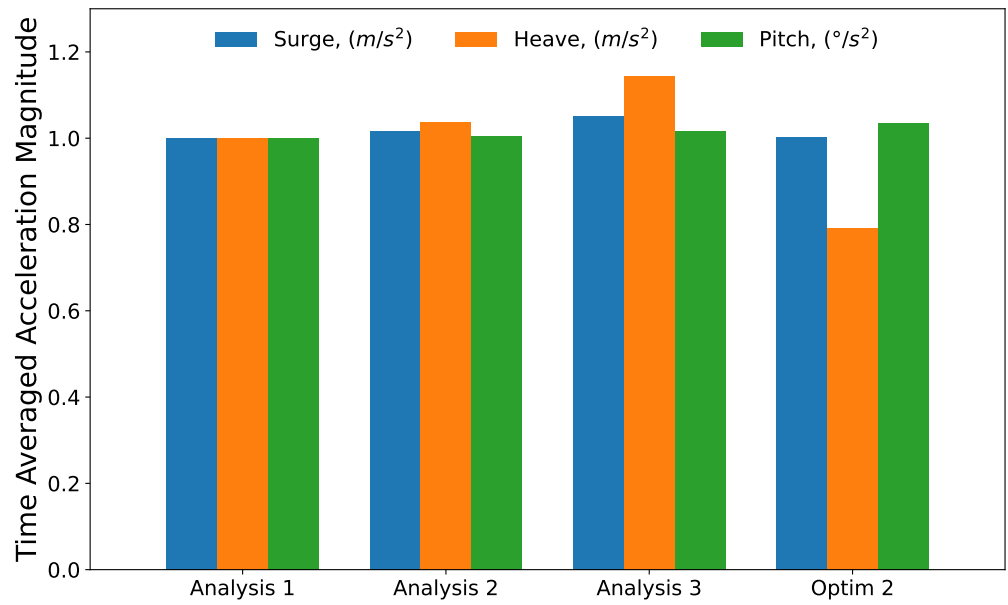DOF

Figure 14: Time-Averaged and Normalized Accelerations for Floating Body Surge, Heave, and Pitch DOF
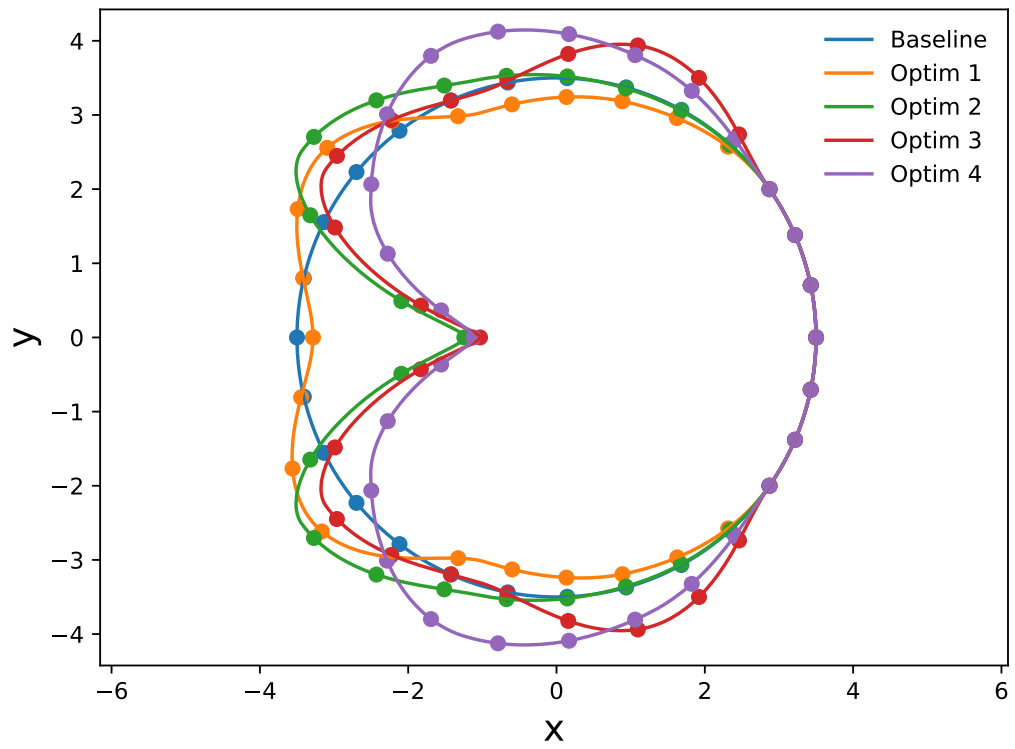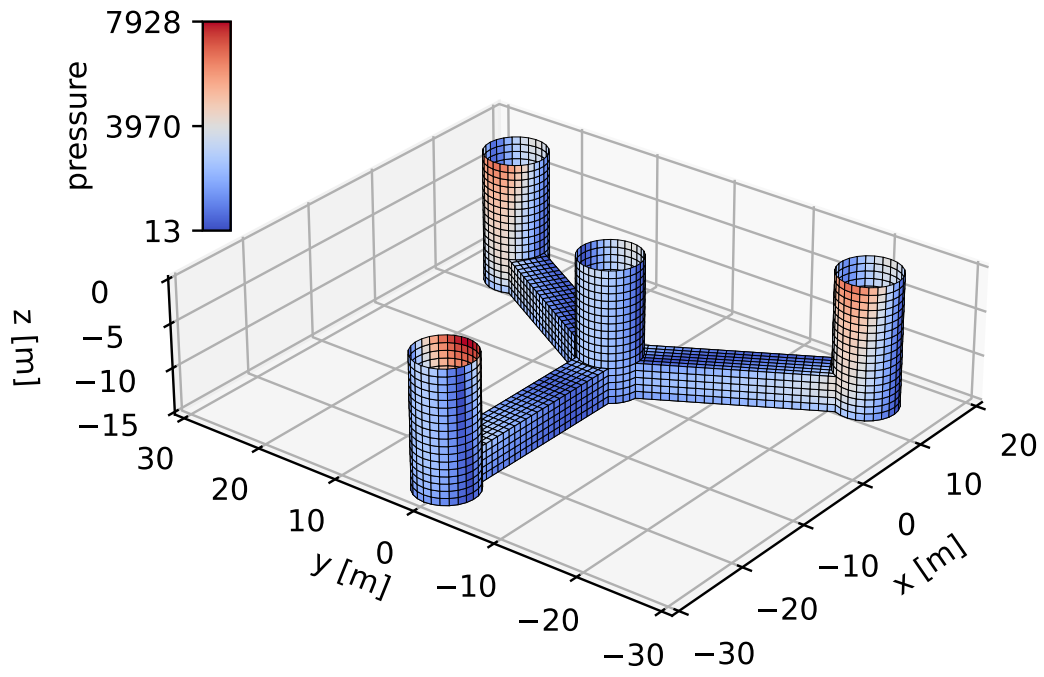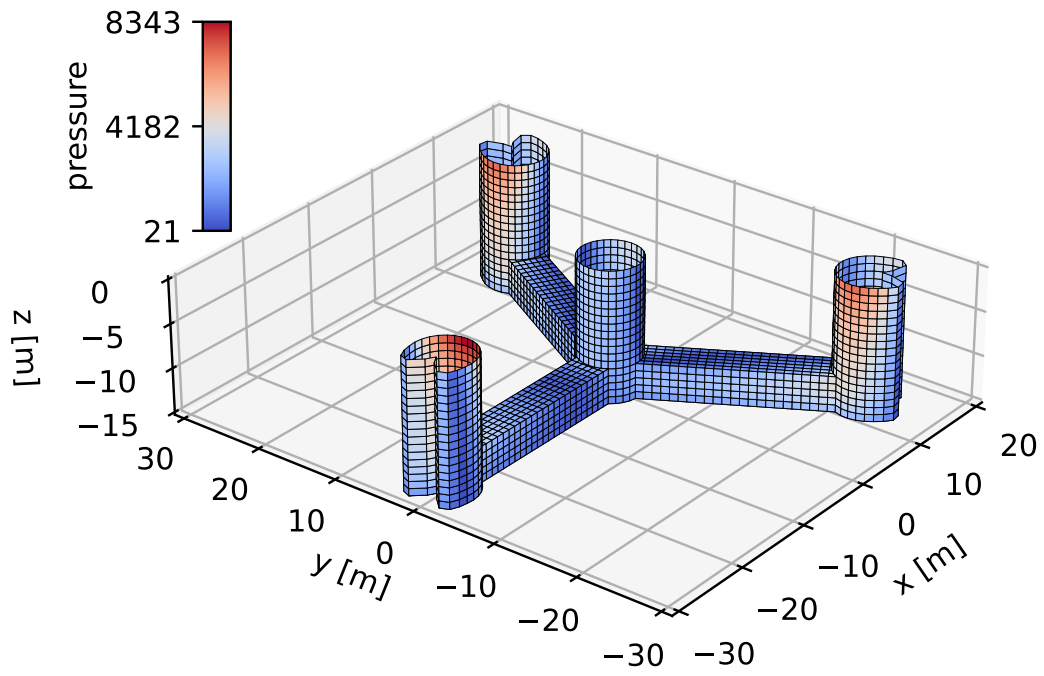
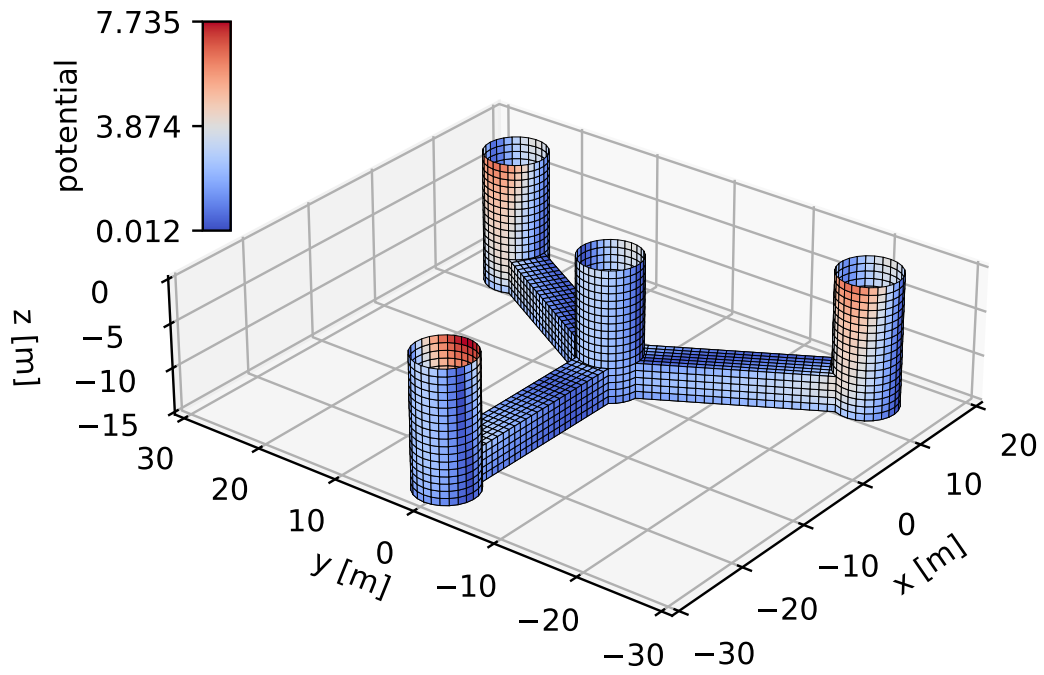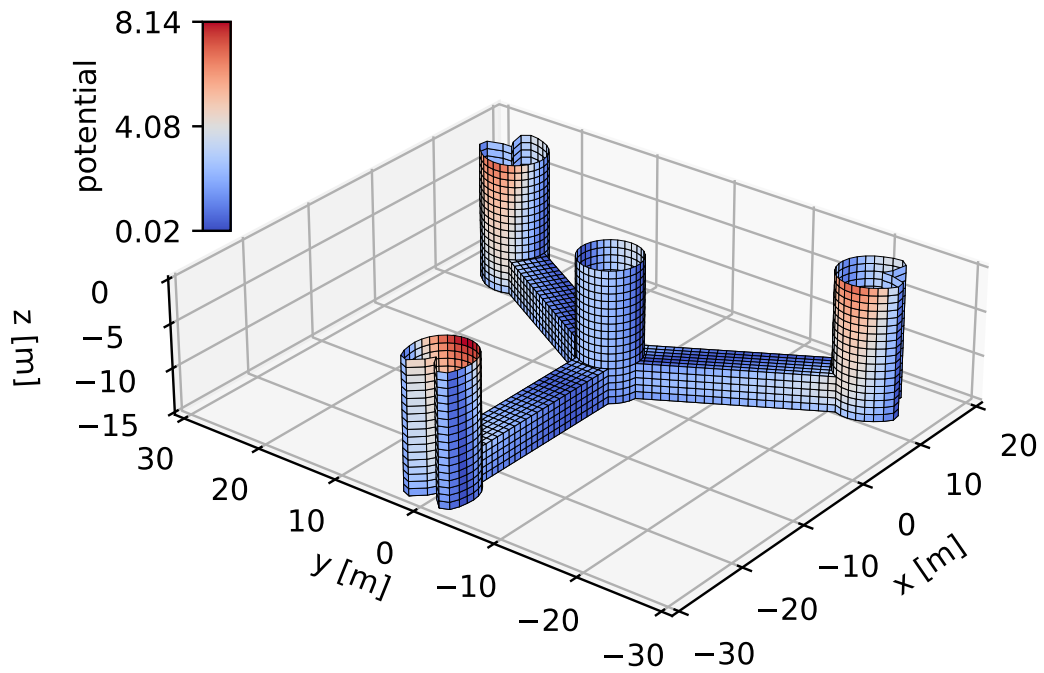Figure 15: Optimal Cross-Sectional Shapes of the Outer Column
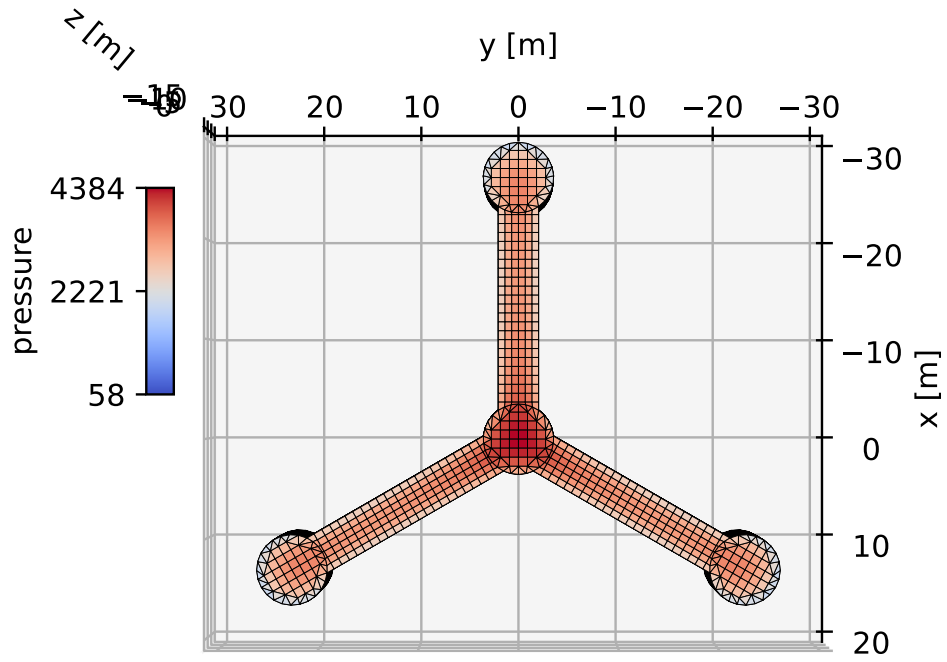
Figure 16: Surge Pressure Field from Radiation Result ($\omega = 1.0$ rad/s)

(a)

(b)

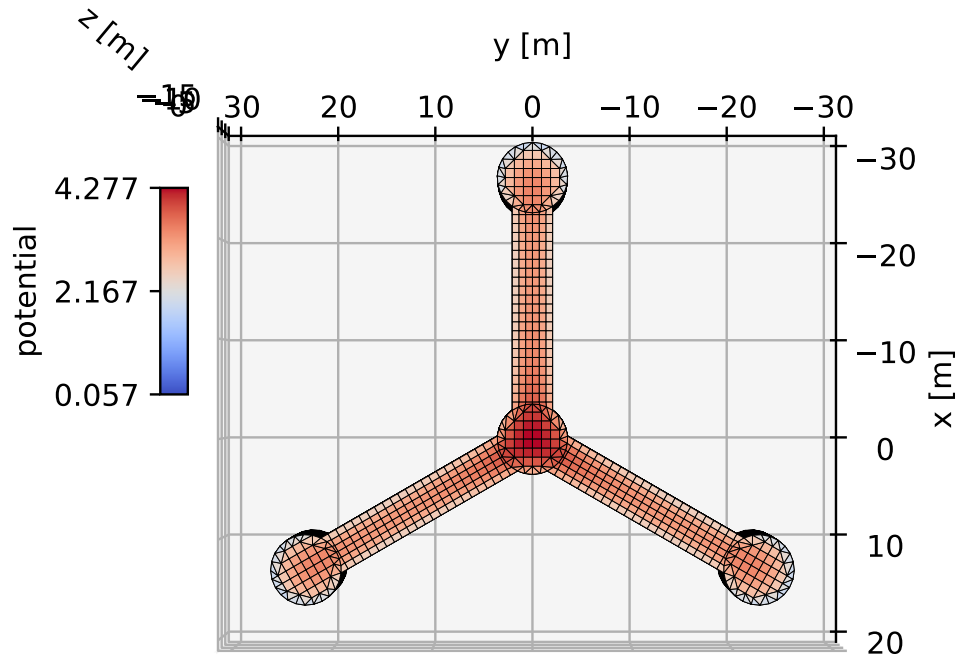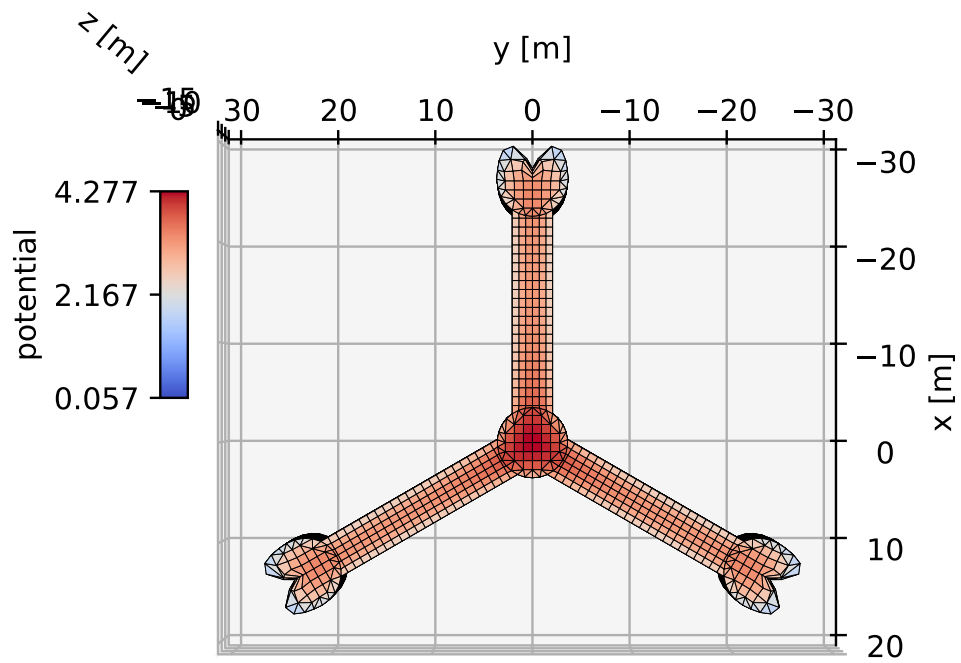Figure 17: Surge Potential Field from Radiation Result ($\omega = 1.0$ rad/s)
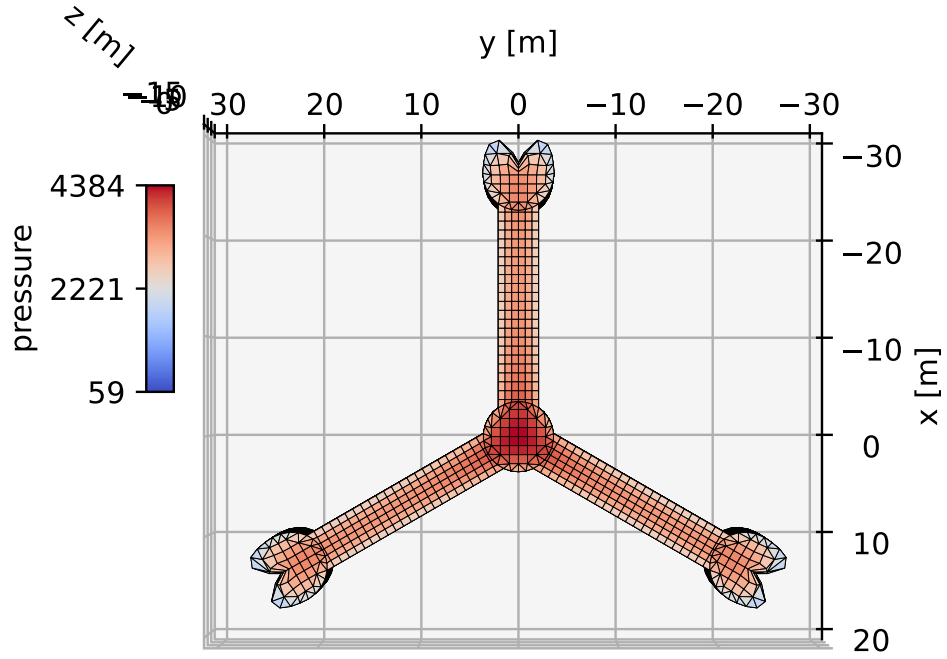
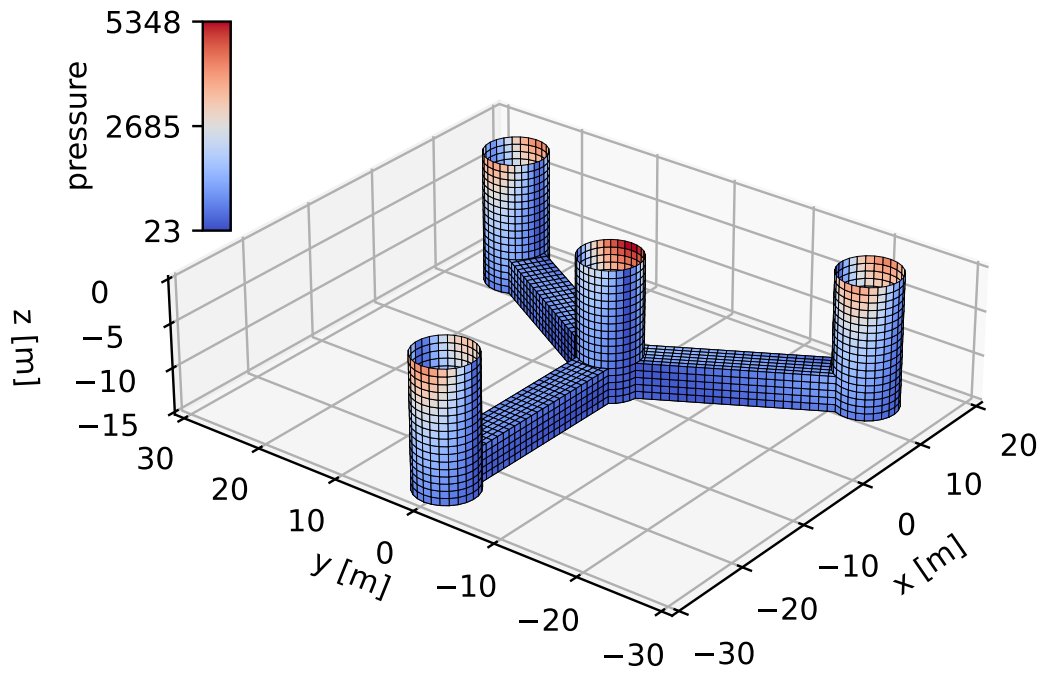Figure 18: Heave Pressure Field from Radiation Result ($\omega = 1.0$ rad/s)
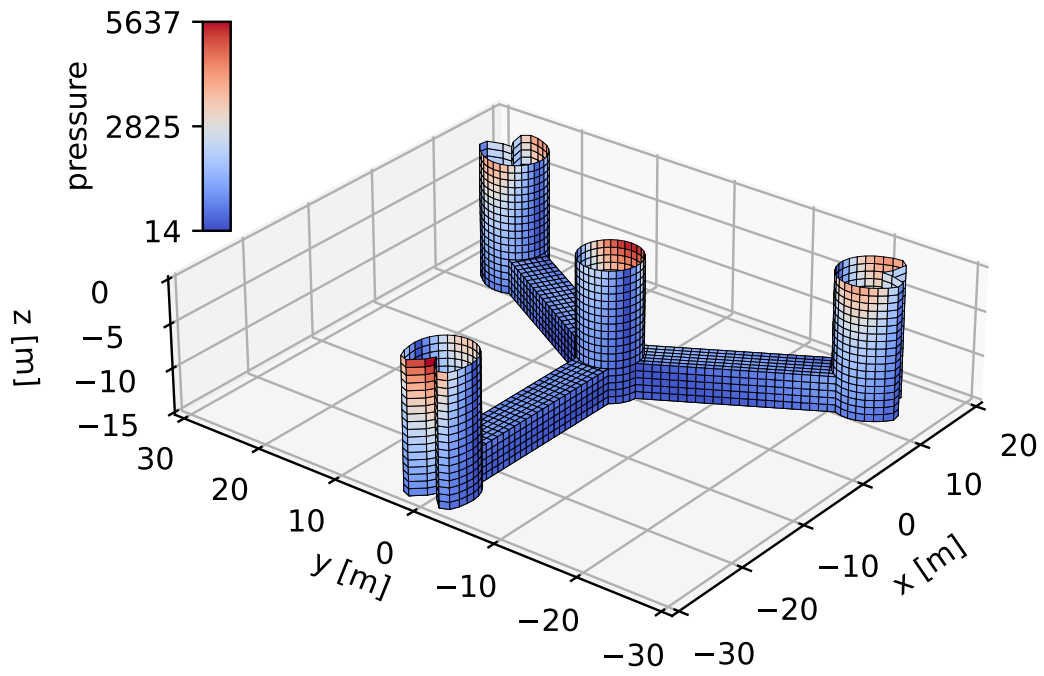
(a)

(b)

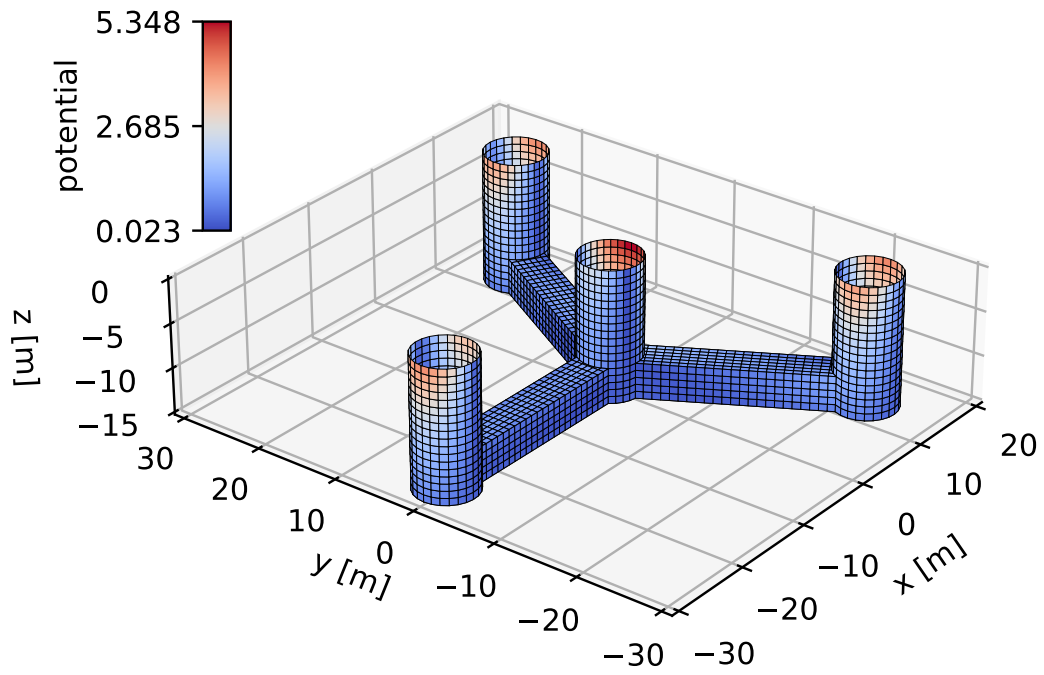Figure 19: Heave Potential Field from Radiation Result ($\omega = 1.0$ rad/s)
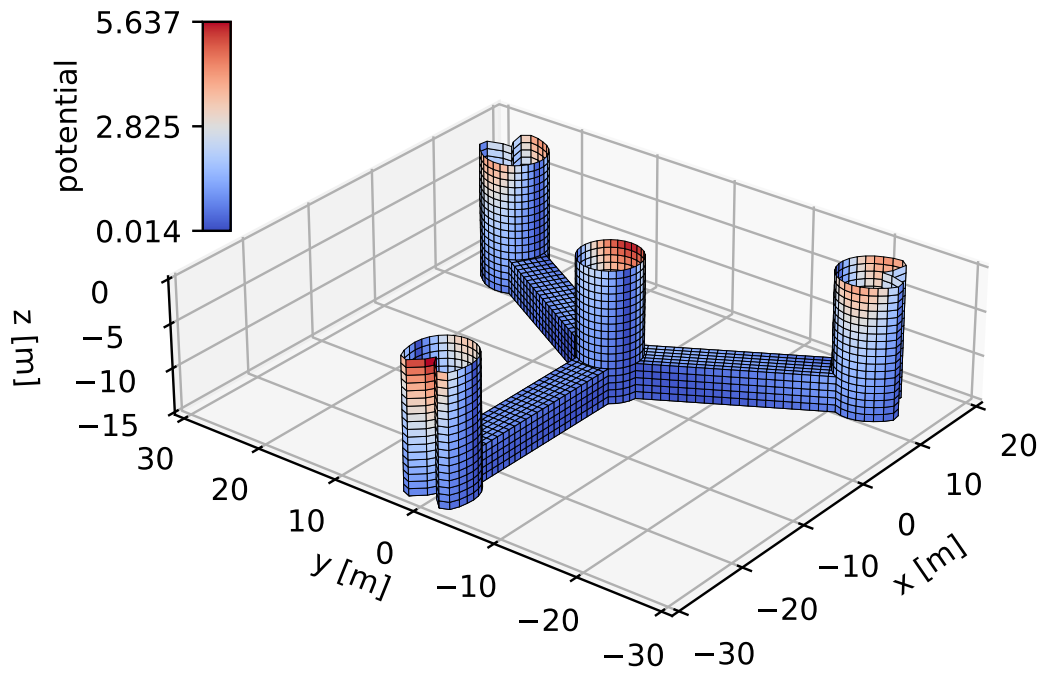
44

(a)

(b)

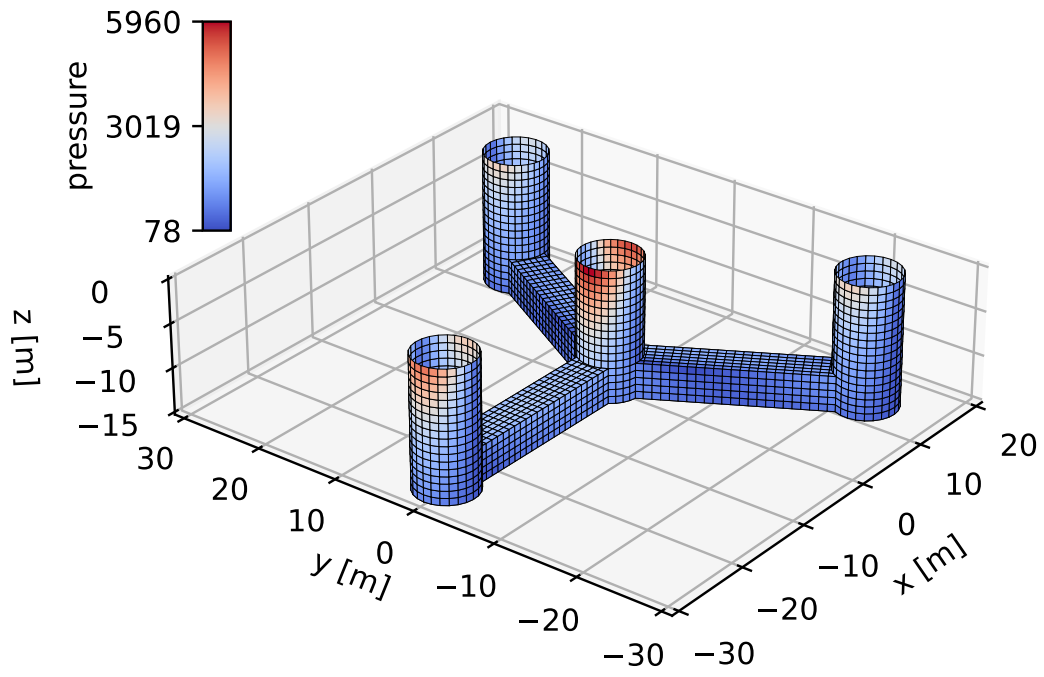Figure 20: Surge Pressure Field from Diffraction Result (wave dir. = 0.0°)
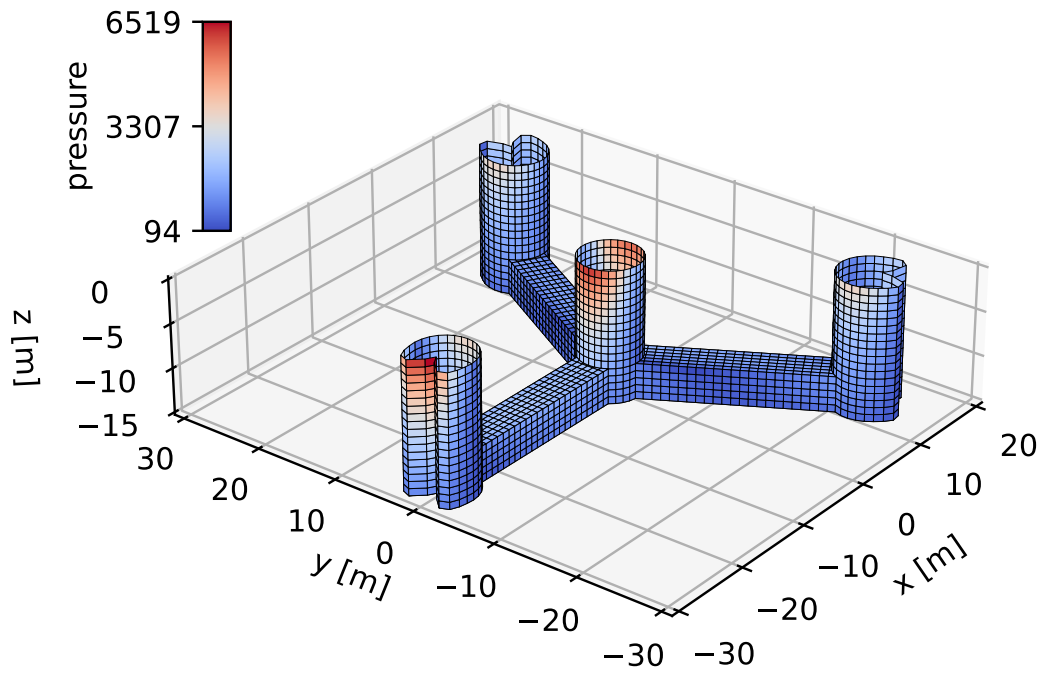
(a)

(b)

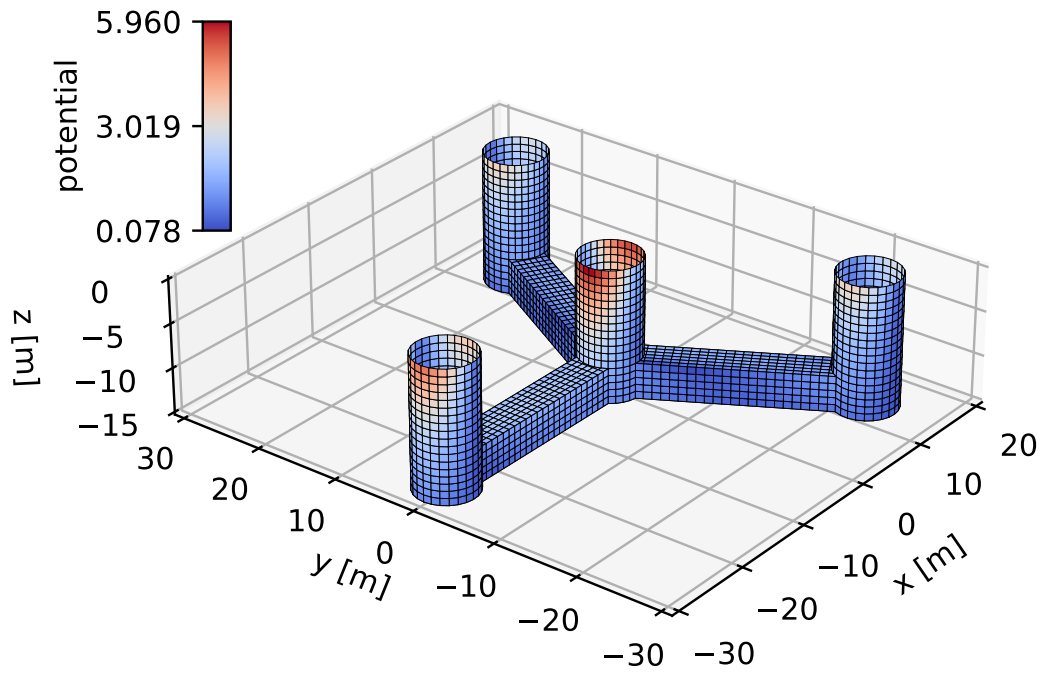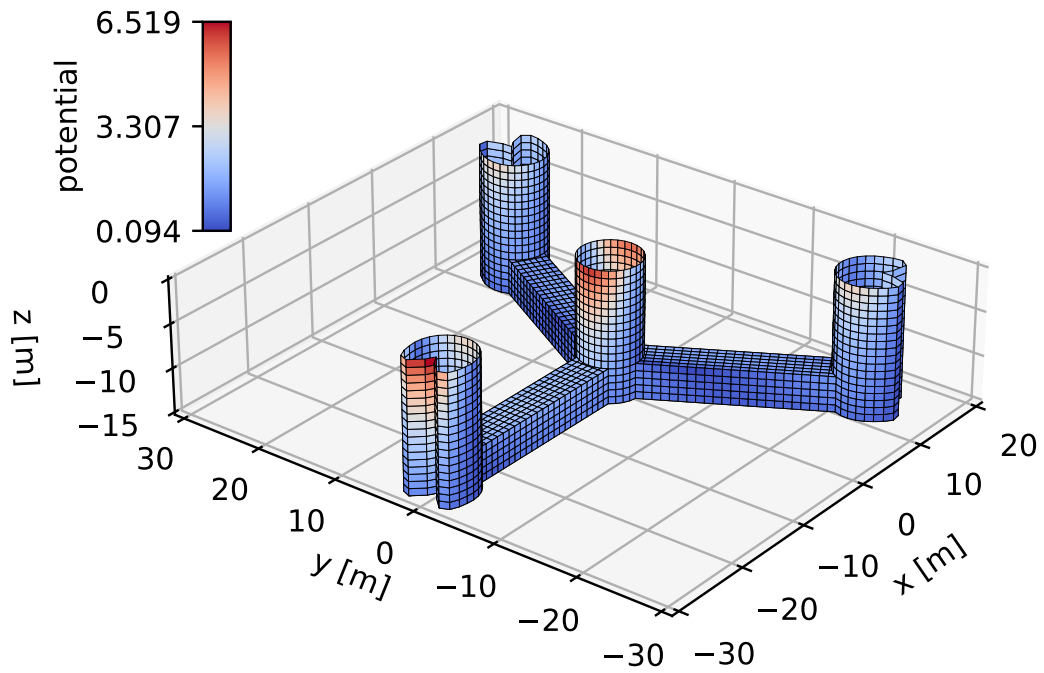Figure 21: Surge Potential Field from Diffraction Result (wave dir. $= 0.0°$)

Figure 22: Heave Pressure Field from Diffraction Result (wave dir. $= 180.0°$)

(a)

(b)

Figure 23: Heave Potential Field from Diffraction Result (wave dir. $= 180.0°$)
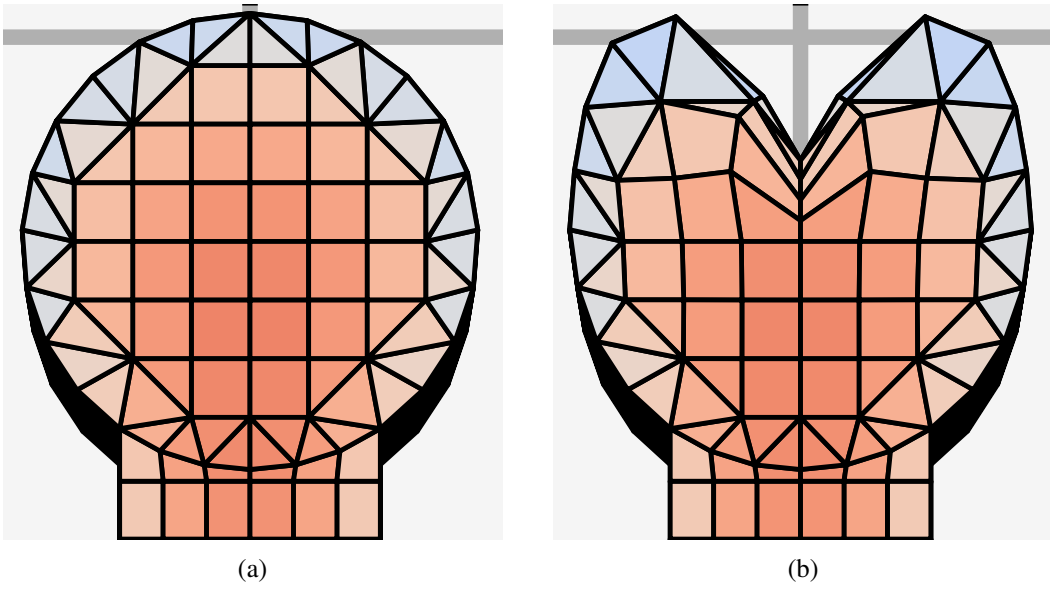
Figure 24: Mesh Distortion

Chapter 5

Conclusion

In this research, the primary objective was to minimize the acceleration profile of a TLP through the use of optimization technique. To do this, the shapes were analyzed over a given time frame to determine the effect of varying loadings placed on the TLP during deployment out on the ocean. This analysis was then repeated for varying shapes by the optimization software to arrive at a more efficient design. After several runs of analysis and varying starting points, a similar shape was reached. All optimization solutions converged to a heart shaped design that created a caved in section for the center with the sides slightly bulging outwards. Because of this unique geometry, the underside of the outer columns reduced the effective heave force due to it mainly being concentrated on the center. By ballooning outwards, this created more area where the TLP was unaffected by heave and thus reduced the overall heave direction. This shape also created the benefit of reducing the pressure field around the center column and focusing it near the outer platforms, reducing the overall stress on the center platform due to loading.

Further studies could employ a full, three dimensional analysis of the TLP by taking into account every node along the outer column individually as it moves up the height of the system. Further refinement to the loadings on the platform could be performed with an increased number of wave loading frequencies and directions. With production playing a vital role in the deployment of TLPs and could be given greater importance during the optimization phase.

Although the data supports all the claims made in this paper, experimental determination of the data had not been performed as of the time of this research. This leaves plenty of room for experimental determination of the physical properties of the heart shaped floating platform and directly comparing it to the original circular floating platform.

The data gained from this analysis had helped to form a more cohesive understanding of overall loading on a TLP and how to further increase their effectiveness when deployed in the field. The decreased heave motion and acceleration profile shows that the new TLP design can

endure harsher loadings while maintaining directional stability while the wind turbine generates power. With this increase there is a larger incentive for TLPs to be adopted in the industry and further incentive to further analyze the floating platform shape.

References

[1] A. Gani, Fossil fuel energy and environmental performance in an extended stirpat model, Journal of Cleaner Production 297 (3) (2021) 0959–6526. `doi:10.1016/j.jclepro.2021.126526`.

[2] R. H. Wiser, Green power marketing: Increasing customer demand for renewable energy, Utilities Policy 7 (1) (1998) 107–119. `doi:10.1016/S0957-1787(98)00005-8`.

[3] M. Hasanuzzaman, U. S. Zubir, N. I. Ilham, H. Seng Che, Global electricity demand, generation, grid system, and renewable energy polices: A review, WIREs Energy and Environment 6 (2) (2017) e222. `doi:10.1002/wene.222`.

[4] J. L. Holechek, H. M. E. Geli, M. N. Sawalhah, R. Valdez, A global assessment: Can renewable energy replace fossil fuels by 2050?, Sustainability 14 (8) (2022) 4792. `doi:10.3390/su14084792`.

[5] Z. Gao, H. Bingham, R. Nicolls-Lee, et al., Issc committee v.4: Offshore renewable energy - discussion, in: International Ship and Offshore Structures Congress, Vol. 3, Cascais, Portugal, 2015, pp. 247–263.

[6] C. V. C. Weiss, R. Guanche, B. Ondiviela, O. F. Castellanos, J. Juanes, Marine renewable energy potential: A global perspective for offshore wind and wave exploitation, Energy Conversion and Management 177 (2018) 43–54. `doi:10.1016/j.enconman.2018.09.059`.

[7] M. Schwartz, D. Heimiller, S. Haymes, W. Musial, Assessment of offshore wind energy resources for the united states, Tech. Rep. NREL/TP-500-45889, National Renewable Energy Laboratory, Golden, CO (6 2010). `doi:10.2172/983415`.

[8] IEA, Renewable energy market update, Tech. rep., International Energy Agency, Paris (6 2023).
URL `https://www.iea.org/reports/renewable-energy-market-update-june-2023`

[9] B. Hélène, F. Marjolaine, L. G. Christelle, P. Le Floc'h, Vulnerability and spatial competition: The case of fisheries and offshore wind projects, Ecological Economics 197 (2022) 107454. `doi:10.1016/j.ecolecon.2022.107454`.

[10] B. Johnston, A. Foley, J. Doran, T. Littler, Levelised cost of energy, a challenge for offshore wind, Renewable Energy 160 (2020) 876–885. `doi:10.1016/j.renene.2020.06.030`.

[11] M. Garcia-Sanz, A metric space with LCOE isolines for research guidance in wind and hydrokinetic energy systems, Wind Energy 23 (2) (2019) 291–311. `doi:10.1002/we.2429`.

[12] S. Xu, S. Wang, C. Guedes Soares, Review of mooring design for floating wave energy converters, Renewable and Sustainable Energy Reviews 111 (2019) 595–621. `doi: 10.1016/j.rser.2019.05.027`.

[13] V. Sykes, M. Collu, A. Coraddu, A review and analysis of the uncertainty within cost models for floating offshore wind farms, Renewable and Sustainable Energy Reviews 186 (1) (2023) 113634. `doi:10.1016/j.rser.2023.113634`.

[14] F. Harris, H. G. Knox, Important considerations in marine construction, Transactions of the AIME 179 (1) (1949) 40–51. `doi:10.2118/949040-G`.

[15] G. Liu, H. Li, Offshore Platform Integration and Floatover Technology, Springer, Singapore, 2017. `doi:10.1007/978-981-10-3617-0`.

[16] N. Wei, Z. Zhang, X. Xu, W. Yao, Stability analysis of a TLP with inclined tension legs under different marine survival conditions, Journal of Marine Science and Engineering 10 (8) (2022) 1058. `doi:10.3390/jmse10081058`.

[17] Y. Han, C. Le, H. Ding, et al., Stability and dynamic response analysis of a submerged tension leg platform for offshore wind turbines, Ocean Engineering 129 (2017) 68–82. `doi:10.1016/j.oceaneng.2016.10.048`.

[18] K. Sadeghi, H. Tozan, Tension leg platforms: An overview of planning, design, construction and installation, Academic Research International 9 (2018) 55–65.

[19] C. Carpenter, Evolution of the tension leg platform, Journal of Petroleum Technology 72 (09) (2020) 72–73. `doi:10.2118/0920-0072-JPT`.

[20] J. Halkyard, Floating offshore platform design, in: Handbook of Offshore Engineering, Elsevier, London, UK, 2005, Ch. 7, pp. 419–661. `doi:10.1016/B978-008044381-2.50010-2`.

[21] Z. Ma, N. Ren, Y. Wang, et al., A comprehensive study on the serbuoys offshore wind tension leg platform coupling dynamic response under typical operational conditions, Energies 12 (11) (2019) 2067. `doi:10.3390/en12112067`.

[22] Y. H. Lee, J. K. Schuh, R. H. Ewoldt, J. T. Allison, Enhancing full-film lubrication performance via arbitrary surface texture design, Journal of Mechanical Design 139 (5) (2017) 053401. `doi:10.1115/1.4036133`.

[23] X. He, J. Li, C. A. Mader, A. Yildirim, J. R. R. A. Martins, Robust aerodynamic shape optimization—from a circle to an airfoil, Aerospace Science and Technology 87 (2019) 48–61. `doi:10.1016/j.ast.2019.01.051`.

[24] C. S. Cain, Y. H. Lee, Hydro-structural design exploration of floating platform for offshore energy systems, in: ASME International Mechanical Engineering Congress and Exposition, no. IMECE2023-112479, New Orleans, LA, 2023, pp. 1–8. `doi:10.1115/IMECE2023-112479`.

[25] R. Wiser, M. Bolinger, 2018 wind technologies market report, Tech. rep., U.S. Department of Energy (2019).
URL https://www.energy.gov/eere/wind/articles/2018-wind-technologies-market-report

[26] S. Wang, Y. Huang, L. Li, et al., Dynamic analysis of wind turbines including nacelle–tower–foundation interaction for condition of incomplete structural parameters, Advances in Mechanical Engineering 9 (3) (2017) 1–17. doi:10.1177/1687814017692940.

[27] A. Abraham, T. Dasari, J. Hong, Effect of turbine nacelle and tower on the near wake of a utility-scale wind turbine, Journal of Wind Engineering and Industrial Aerodynamics 193 (2019) 103981. doi:10.1016/j.jweia.2019.103981.

[28] N. Kang, S. C. Park, J. Park, S. N. Atluri, Dynamics of flexible tower-blade and rigid nacelle system: dynamic instability due to their interactions in wind turbine, Journal of Vibration and Control 22 (3) (2016) 826–836. doi:10.1177/1077546314532119.

[29] N. N. Hoang Quan, P. V. Lam, L. V. Long, Wind turbine blade design optimization using OpenFOAM and DAKOTA software, Transportation Research Procedia 56 (2021) 71–78. doi:10.1016/j.trpro.2021.09.009.

[30] R. Vaidhye, R. Banapurkar, P. V. Jadhav, Blade design and performance analysis of wind turbine, International Journal for Research in Applied Science & Engineering Technology (IJRASET) 10 (2022) 2220–2227. doi:10.22214/ijraset.2022.44217.

[31] K. A. Adeyeye, N. Ijumba, J. Colton, The effect of the number of blades on the efficiency of a wind turbine, IOP Conference Series: Earth and Environmental Science 801 (1) (2021) 012020. doi:10.1088/1755-1315/801/1/012020.

[32] J. Solano, T. Montaño, J. Maldonado-Correa, A. Ordóñez, M. Pesantez, Correlation between the wind speed and the elevation to evaluate the wind potential in the southern region of ecuador, Energy Reports 7 (2021) 259–268. doi:10.1016/j.egyr.2021.06.044.

[33] J. Kaldellis, M. Kapsali, Shifting towards offshore wind energy—recent activity and future development, Energy Policy 53 (2013) 136–148. doi:https://doi.org/10.1016/j.enpol.2012.10.032.

[34] R. Künneke, D. C. Mehos, R. Hillerbrand, K. Hemmes, Understanding values embedded in offshore wind energy systems: Toward a purposeful institutional and technological design, Environmental Science & Policy 53 (2015) 118–129. doi:10.1016/j.envsci.2015.06.013.

[35] G. E. Barter, L. Sethuraman, P. Bortolotti, et al., Beyond 15 MW: A cost of energy perspective on the next generation of drivetrain technologies for offshore wind turbines, Applied Energy 344 (2023) 121272. doi:10.1016/j.apenergy.2023.121272.

[36] T. A. Hansen, E. J. Wilson, J. P. Fitts, M. Jansen, et al., Five grand challenges of offshore wind financing in the united states, Energy Research & Social Science 107 (2024) 103329. `doi:10.1016/j.erss.2023.103329`.

[37] M. Karimirad, Fixed offshore wind turbines, in: Offshore Energy Structures, Springer, 2014, pp. 23–52. `doi:10.1007/978-3-319-12175-8_3`.

[38] L. Wang, A. Kolios, X. Liu, D. Venetsanos, R. Cai, Reliability of offshore wind turbine support structures: A state-of-the-art review, Renewable and Sustainable Energy Reviews 161 (2022) 112250. `doi:10.1016/j.rser.2022.112250`.

[39] C. V. Amaechi, A. Reda, H. O. Butler, I. A. Ja'e, C. An, Review on fixed and floating offshore structures. part I: Types of platforms with some applications, Journal of Marine Science and Engineering 10 (8) (2022) 2067. `doi:10.3390/jmse10081074`.

[40] E. C. Edwards, A. Holcombe, S. Brown, et al., Evolution of floating offshore wind platforms: A review of at-sea devices, Renewable and Sustainable Energy Reviews 183 (2023) 113416. `doi:10.1016/j.rser.2023.113416`.

[41] S. Bashetty, S. Ozcelik, Review on dynamics of offshore floating wind turbine platforms, Energies 14 (19) (2021) 6026. `doi:10.3390/en14196026`.

[42] NREL, The leading edge: April 2020 wind energy newsletter, `https://www.nrel.gov/wind/newsletter-202004.html`, accessed: 12/03/2023 (2020).

[43] E. Uzunoglu, E. Oguz, C. Guedes Soares, An overview of platform types used in floating wind energy, in: International Congress on Ship and Marine Technology, Istanbul, Turkey, 2021, pp. 51–63.

[44] M. Palraj, P. Rajamanickam, Motion control studies of a barge mounted offshore dynamic wind turbine using gyrostabilizer, Ocean Engineering 237 (2021) 109578. `doi:10.1016/j.oceaneng.2021.109578`.

[45] A. Alkhalidi, H. Kaylani, N. Alawawdeh, Technology assessment of offshore wind turbines: Floating platforms – validated by case study, Results in Engineering 17 (2023) 100831. `doi:10.1016/j.rineng.2022.100831`.

[46] G. Ferri, E. Marino, C. Borri, Optimal dimensions of a semisubmersible floating platform for a 10 MW wind turbine, Energies 13 (12) (2020) 3092. `doi:10.3390/en13123092`.

[47] E. E. Bachynski, T. Moan, Design considerations for tension leg platform wind turbines, Marine Structures 29 (1) (2012) 89–114. `doi:10.1016/j.marstruc.2012.09.001`.

[48] J. Paulling, E. Horton, Analysis of the tension leg platform, Society of Petroleum Engineers Journal 11 (03) (1971) 285–294. `doi:10.2118/3141-PA`.

[49] R. Mitra, A. Banik, S. Chatterjee, State feedback control of surge oscillations of two-point mooring system, Journal of Sound and Vibration 386 (2017) 1–20. `doi:10.1016/j.jsv.2016.07.038`.

[50] N. Haritos, Introduction to the analysis and design of offshore structures–an overview, Electronic Journal of Structural Engineering 7 (2007) 55–65. `doi:10.56748/ejse.651`.

[51] S. J. Leverette, S. B. Hodges, The tension leg platform: from Hutton to Big Foot, in: OTC Offshore Technology Conference, 2020, p. D021S017R003. `doi:10.4043/30752-MS`.

[52] S. Chakrabarti, J. Halkyard, C. Capanoglu, Historical development of offshore structures, in: Handbook of Offshore Engineering, Elsevier, London, UK, 2005, Ch. 1, pp. 1–38. `doi:10.1016/B978-008044381-2.50004-7`.

[53] X. Xu, N. Wei, W. Yao, The stability analysis of tension-leg platforms under marine environmental loads via altering the connection angle of tension legs, Water 14 (3) (2022) 283. `doi:10.3390/w14030283`.

[54] J. Murert, P. Flugstad, B. Greiner, R. D'Souza, I. C. Solber, The 3 column TLP – a cost efficient deepwater production and drilling platform, in: Offshore Technology Conference, no. OTC-8045-MS, Houston, TX, 1996. `doi:10.4043/8045-MS`.

[55] M. Al-Rawajfeh, M. Gomaa, Comparison between horizontal and vertical axis wind turbine, International Journal of Applied Power Engineering 12 (2023) 13–23. `doi:10.11591/ijape.v12.i1.pp13-23`.

[56] R. P. Nordgren, The design of tension leg platforms by a constrained optimization method, Journal of Offshore Mechanics and Arctic Engineering 111 (3) (1989) 194–202. `doi:10.1115/1.3257147`.

[57] M. E. H. Al-Kharbosy, Enhancement protection and operation of the doubly fed induction generator during grid fault, Master's thesis, South Valley University, Qena, Egypt (04 2012).

[58] V. Jaksic, C. Wright, A. Chanayil, S. F. Ali, et al., Performance of a single liquid column damper for the control of dynamic responses of a tension leg platform, Journal of Physics Conference Series 628 (2015) 012058. `doi:10.1088/1742-6596/628/1/012058`.

[59] G. Fulton, D. Malcolm, H. Elwany, et al., Semi-submersible platform and anchor foundation systems for wind turbine support, Tech. rep., National Renewable Energy Laboratory (NREL) (2007).
URL `https://www.nrel.gov/docs/fy08osti/40282.pdf`

[60] H. Suzuki, Y. Kitahara, Y. Fukumoto, Progressive drift of moored floating wind turbines in a wind farm: Improved mooring capacity model, in: ASME International Conference on Offshore Mechanics and Arctic Engineering, Vol. 5, 2011, pp. 83–88. `doi:10.1115/OMAE2011-49730`.

[61] Z. Zhao, W. Wang, W. Shi, X. Li, Effects of second-order hydrodynamics on an ultra-large semi-submersible floating offshore wind turbine, Structures 28 (2020) 2260–2275. `doi:10.1016/j.istruc.2020.10.058`.

[62] M. Horoub, Dynamic analysis of a tension leg platforms (TLPs) subjected to sea wave loads, IEEE Access 99 (2020) 35222–35230. `doi:10.1109/ACCESS.2020.2971903`.

[63] A. Doerry, Ship dynamics for maritime isar imaging, Tech. rep., Sandia National Laboratories (02 2008). `doi:10.2172/929523`.

[64] C. Li, J. M. Mogollón, A. Tukker, J. Dong, D. von Terzi, C. Zhang, B. Steubing, Future material requirements for global sustainable offshore wind energy development, Renewable and Sustainable Energy Reviews 164 (2022) 112603. `doi:10.1016/j.rser.2022.112603`.

[65] M. Ancellin, F. Dias, Capytaine: a Python-based linear potential flow solver, Journal of Open Source Software 4 (36) (2019) 1341. `doi:10.21105/joss.01341`.

[66] Y. H. Lee, S. Y. Boo, J. T. Allison, A framework for integrating hydrostatics, hydrodynamics, and rigid-body dynamics for the control co-design of floating offshore vertical-axis wind turbine systems, in: Wind Energy Science Conference, Hannover, Germany, 2021.

[67] H. T. Wist, Statistical properties of successive ocean wave parameters, Ph.D. thesis, Norwegian University of Science and Technology (2003).
URL `http://hdl.handle.net/11250/227925`